Geochimica et Cosmochimica Acta 427 (2026) 497–515

Contents lists available at ScienceDirect

Geochimica et Cosmochimica Acta

journal homepage: www.elsevier.com/locate/gca

Environmental and vital effects on lithium isotopes and trace element ratios in biogenic carbonates: Insights from an estuarine salinity gradient☆

Alexandra M. Schaffer [a,*], Gordon D.Z. Williams [a], Gary S. Dwyer [a], Ethan G. Hyland [b], Juliet M. Wong [c], Joshua S. Osterberg [c], Thomas F. Schultz [c], Michael A. Kipp [a]

[a] Division of Earth and Climate Sciences, Nicholas School of the Environment, Duke University, Durham, NC 27708, United States
[b] Department of Marine, Earth, and Atmospheric Sciences, North Carolina State University, Raleigh, NC 27695, United States
[c] Division of Marine Science and Conservation, Nicholas School of the Environment, Duke University Marine Lab, Beaufort, NC 28516, United States

ARTICLE INFO

Co-Guest Editor: Philip Pogge von Strandmann

Keywords:
Crassostrea virginica
Estuary
Calcite
Aragonite
Lithium
Magnesium
Calcium

ABSTRACT

Isotope and element ratios in the carbonate skeletons of calcifying marine organisms can be used to reconstruct past environments and understand physiological processes occurring before calcification. The Li isotope composition (δ^7Li) of biogenic carbonates is thought to reflect the δ^7Li values of the water in which the calcifying organisms grew, allowing for the use of carbonate fossils to estimate δ^7Li of ancient seawater, which is known to record past silicate rock weathering congruency. To determine whether δ^7Li in biogenic carbonates is truly a faithful archive of past seawater, it is crucial to elucidate any environmental or biological factors that could influence carbonate δ^7Li and cause deviations from seawater δ^7Li. Here we show that δ^7Li in the low-Mg calcite shell of the eastern oyster, *Crassostrea virginica*, tracks aqueous δ^7Li with an offset of +1.9 ± 1.5‰ and is not influenced by salinity in an estuarine environment. This contrasts with inorganic calcite, in which δ^7Li is known to be lower than seawater values, suggesting a prevalent vital effect in oyster calcite. We ascribe this vital effect to a combination of possible physiological isotope fractionation mechanisms, including preferential passive removal of ^{6}Li from the extrapallial fluid (EPF) and preferential transport of ^{6}Li into the EPF via a Na^+/H^+ pump, both of which have been discussed by previous studies. Overall, we conclude that understanding the mechanism (s) driving the vital effect in biogenic calcite is crucial to establishing δ^7Li as a faithful paleo-archive and a tool for reconstructing past weathering and climate.

1. Introduction

A growing fascination of geochemists, lithium (Li) isotope systematics have garnered interest as a paleoceanographic proxy (Chan and Edmond, 1988; Chan et al., 1992; Misra and Froelich, 2012; Pogge von Strandmann et al., 2017). Fluvial or estuarine Li isotope composition ($\delta^7Li = ((^7Li/^6Li)_{sample}/(^7Li/^6Li)_{standard}) - 1) \times 1000$) can be used to construct silicate weathering congruency, or the ratio of primary silicate mineral dissolution to secondary mineral formation. This traces silicate weathering intensity, or the ratio of weathering rate to erosion rate, which is a key paleoclimate parameter that dictates the strength of Earth's silicate weathering 'thermostat' (*e.g.*, Misra and Froelich, 2009; Pogge von Strandmann et al., 2017, 2020).

With a range of +1 to +44‰ (Pogge von Strandmann et al., 2006; Dellinger et al., 2015; Murphy et al., 2019), dissolved fluvial δ^7Li values are typically greater than those of the upper continental crust (−5 to +5‰) (Teng et al., 2004) and vary between basins with unique lithologies and silicate weathering congruencies (Huh et al., 1998; Millot et al., 2010). Seawater, in contrast, has a globally homogenous modern δ^7Li value of +31‰ (Millot et al., 2004). With an oceanic residence time of ~1.2 million years (Broecker and Peng, 1982), Li behaves conservatively in seawater and exists in concentrations proportional to salinity at around 180 ppb (Tomascak et al., 2016; Millero, 2016) – much higher than riverine Li concentrations, which vary regionally but average globally at 1.5 ppb (Huh et al., 1998). As Li-poor rivers flow into brackish environments and interact with Li-rich seawater, fluvial δ^7Li values representative of local continental silicate weathering congruency are mixed into the global ocean composition. Therefore, fluvial and brackish environments that retain significant riverine input are suitable systems to measure δ^7Li as a proxy for regional silicate weathering

☆ This article is part of a special issue entitled: 'Geochemical Proxies_Zhang' published in Geochimica et Cosmochimica Acta.

* Corresponding author.
E-mail address: lexi.schaffer@duke.edu (A.M. Schaffer).

https://doi.org/10.1016/j.gca.2026.06.025
Received 15 December 2025; Accepted 16 June 2026
Available online 22 June 2026

dynamics, while the isotopic composition of global mean seawater tracks the globally integrated silicate weathering congruency along with hydrothermal flux and weathering of mid-ocean ridge basalts (Chan et al., 1992; Huh et al., 1998; Misra and Froelich, 2012; Pogge von Strandmann et al., 2017).

Ideally, pristine inorganic and biogenic calcium carbonates ($CaCO_3$) retain the δ^7Li values of the surrounding fluvial, estuarine, or marine water at the time and place of growth, serving as paleo-proxies for silicate weathering and other environmental conditions. Like other alkali metal ions, Li^+ is incorporated interstitially in calcite and substitutes for calcium ions (Ca^{2+}) in the crystal structure of aragonite (Okumura and Kitano, 1986). After initial incorporation, diagenesis can influence δ^7Li and other geochemical signatures in carbonates (Ullmann and Korte, 2015; Dellinger et al., 2020; Murphy et al., 2022). This effect is less pronounced in calcite than in aragonite because calcite has a more stable crystal structure (Veizer, 1983; Marshall, 1992; Morse et al., 2007). Diagenesis in low-magnesium (Mg) calcite (< 4 mol% $MgCO_3$; Chave, 1962) can be screened for using element ratio proxies, such as the manganese-to-calcium ratio (Mn/Ca) (*e.g.*, Korte et al., 2009; Korte and Hesselbo, 2011), the iron-to-calcium ratio (Fe/Ca) (*e.g.*, Jones et al., 1994; Wierzbowski and Joachimski, 2007), and the strontium-to-calcium ratio (Sr/Ca) (*e.g.*, Korte et al., 2009; Korte and Hesselbo, 2011). These screening methods are summarized by Ullman and Korte (2015) and discussed with respect to this study in Section 4.3.

Modern biogenic carbonates have δ^7Li values ranging from +15 to +40‰, reflecting strong intra-species, inter-species, and environmental variability (Dellinger et al., 2018). Dellinger et al. (2018) highlighted this variability by measuring δ^7Li in brachiopods (+25 to +28‰), echinoderms (constant at about 24‰), aragonite mollusks (+15 to +22‰), and calcite mollusks (+25 to +40‰) and reporting previous measurements of δ^7Li in corals (+17 to +25‰, Marriott et al., 2004a, 2004b; Rollion-Bard et al., 2009), planktic foraminifera (+27 to +31‰, Marriott et al., 2004a; Hall et al., 2005; Hathorne and James, 2006; Misra and Froelich, 2009; Rollion-Bard et al., 2009), and benthic foraminifera (+25 to +28‰, Marriott et al., 2004b).

As fossils, these taxa have the potential to record the δ^7Li values of the ancient water in which they grew. However, variables such as salinity, temperature, carbonate mineralogy, water composition, growth rate, diagenetic effects and vital effects (biological processes that fractionate isotopes) could influence Li isotope fractionation between the shell and the internal calcifying fluid from which the shell precipitates, or between the calcifying fluid and other internal reservoirs. This could result in a δ^7Li value in the shell that is different from the δ^7Li value of the surrounding water (*e.g.*, Marriott et al., 2004a, 2004b; Vigier et al., 2015; Dellinger et al., 2018, 2020). Therefore, understanding how environmental, biological, and mineralogical variables influence the incorporation of Li in calcifying organisms is critical to determining which taxa, if any, serve as faithful archives of past seawater. To this end, studies have measured the Li isotope composition of a diverse array of biogenic carbonates, revealing that δ^7Li in biogenic aragonite and high-Mg calcite (> 4 mol% MgCO3; Chave, 1962) is lower than seawater δ^7Li (Marriott et al., 2004a; Rollion-Bard et al., 2009; Dellinger et al., 2018), while δ^7Li in biogenic low-Mg calcite ranges from lower to higher than seawater δ^7Li both within and among taxa (Marriott et al., 2004a, 2004b; Misra and Froelich, 2009; Rollion-Bard et al., 2009; Hathorne et al., 2013). Dellinger et al. (2018) found that δ^7Li values in calcite and aragonite mollusks deviate significantly from that of seawater and inorganic carbonates, indicating a vital effect and suggesting that more studies assessing Li isotopes in mollusks are needed to evaluate the potential for this phylum to serve as a paleo-archive for past seawater.

Within the mollusks, oysters grow low-Mg calcite shells with seasonal growth bands that record geochemical information from their lifespan of several years (Mackenzie, 2007). Due to their geological longevity, seasonal resolution, and relatively long lifespans, oysters are a promising candidate for reconstructing δ^7Li values of past estuary water or seawater as paleo-proxies for silicate weathering congruency. To determine whether oyster shells accurately record water δ^7Li, Dellinger et al. (2018) measured δ^7Li in the shell of the Pacific oyster, *Magallana gigas*, and found evidence of vital effects and no temperature dependence. However, δ^7Li values in oyster calcite – and other biogenic carbonates – have yet to be tested for a relationship to salinity, which is a key parameter in estuarine environments that host oysters. Determining the relationship (or lack thereof) between salinity and shell δ^7Li is imperative to evaluating the effectiveness with which Li isotope measurements in fossil estuarine shells may track past water Li isotope composition and potentially serve as a proxy for past silicate weathering congruency.

We addressed this gap in knowledge by measuring δ^7Li in modern low-Mg calcite shells of the eastern oyster, *Crassostrea virginica*, an abundant reef-builder that lives in estuaries and shallow marine environments along much of the eastern coastline of the United States. The oysters measured in this study were collected along an estuarine salinity gradient (20.9–33.0 ppt) in coastal North Carolina. We also measured δ^7Li in water samples collected from the oyster sampling sites to characterize the Li isotope fractionation occurring between the oysters and the water in which they grew. In addition to Li isotopes, we investigated several element ratios that have yet to be studied as a function of salinity in oyster calcite, including Sr/Ca, Li/Ca, Mg/Ca, and Li/Mg, all of which are known to be sensitive to temperature in marine biogenic carbonates (*e.g.*, Delaney et al., 1989; Beck et al., 1992; Butler et al., 2015; Chen D. et al., 2023). Lastly, we measured δ^{18}O and δ^{13}C, the former of which is a temperature proxy in bivalve shells (*e.g.*, Killingley and Berger, 1979; Wefer and Berger, 1991; Andrus and Crowe, 2000; Surge et al., 2001; Ullmann et al., 2010; Bougeois et al., 2016), to substantiate the salinity gradient of our sampling transect. These data allow us to tentatively trace regulation of ions in the calcification reservoir (see Zeebe and Sanyal, 2002; Bentov and Erez, 2006; Dellinger et al., 2018) and inclusion (or exclusion) of ions in the crystal lattice of biogenic calcite (see Berner, 1975; Marriott et al., 2004a, 2004b). By evaluating δ^7Li, several element ratios, and δ^{18}O and δ^{13}C as they relate to salinity in modern oyster shells, we aim to increase the accuracy of Li isotope measurements in biogenic low-Mg calcite as an archive of past seawater and a paleo-proxy for continental silicate rock weathering.

2. Materials and methods

2.1. Sample collection

In November 2024, 49 wild oysters were collected from eight sites (5–8 oysters per site) in the Newport River, Adams Creek, and Bogue Sound in the estuary systems of coastal (Atlantic) North Carolina (Fig. 1). The oysters were collected by hand at ~0.5 m depth. At the time of sampling, the sites ranged in measured salinity from 12.2 to 29.8 ppt, establishing a gradient of increasing salinity with increasing proximity to the Atlantic Ocean. A 500 mL water sample was collected from each site; all water samples were then filtered (0.2 μm pore size) and acidified (0.02 M HCl) in acid-washed HDPE bottles. Water collection and salinity measurements were conducted at the same depth as oyster collection at each site to minimize the impact of vertical variations in water composition. Continuous salinity data were retrieved from two National Park Service Monitoring stations located close to the sites (Fig. 1) to elucidate temporal salinity patterns in the estuary (depth of salinity measurements is not specified in the database). To estimate seasonal variation, salinity was remeasured at each site in August 2025, showing a range of 24.4 to 36.2 ppt. In both November 2024 and August 2025, salinity was measured about halfway between high and low tide with minimal precipitation during the day of sampling and the day prior. The two-point average salinity between November 2024 and August 2025 was calculated for each sampling site (range of 20.9 to 33.0 ppt, shown in Fig. 1) and used for isotope and element ratio analyses.

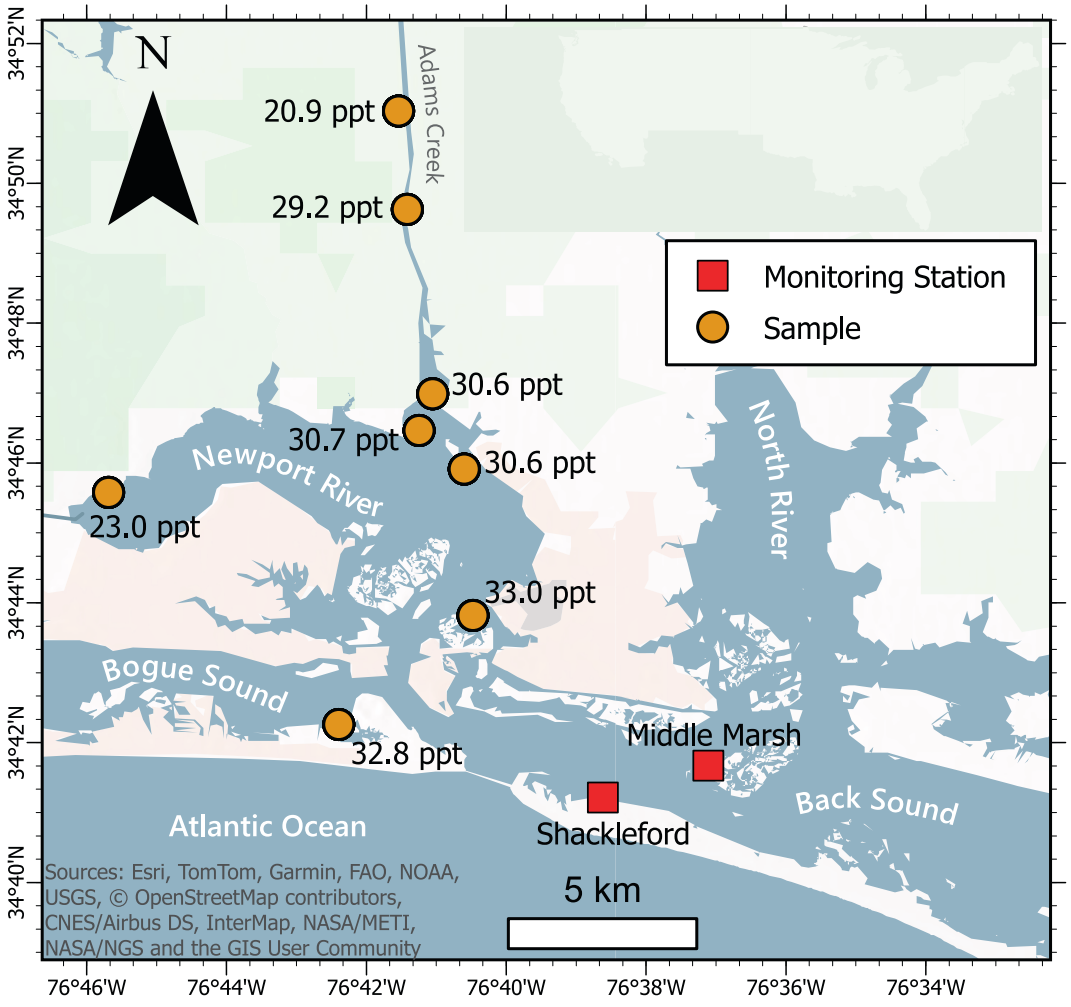

Fig. 1. Map of sample locations. Shown are eight sampling sites from which oysters were collected in November 2024 as well as two monitoring stations: Middle Marsh (34.69452, −76.6185) and Shackleford Banks (34.68692,−76.64364). Two-point average salinity between point measurements taken in November 2024 and August 2025 is labeled at each sampling site. Continuous salinity data were retrieved from the two monitoring stations. Map created with ArcGIS.

2.2. Sample preparation

Within hours of sample collection, the oysters were shucked and the shells were scrubbed clean with a wire brush. The outer layer of the left valve of each shell was abraded with a 32.1 mm diameter diamond wheel bit connected to a Dremel to reduce contamination from external organic matter. Then, using the same Dremel setup, three pieces (each ~1.5 cm^2 in plane of the shell surface and ~0.5 cm thick) were cut out from the left valve: one from close to the umbo, one from the middle of the shell, and one from close to the far lip (Fig. 2). Seasonality and variations in environmental factors such as wave energy (Ortega, 1981) and substrate material (Dunn et al., 2014) can significantly change *C. virginica* growth rate, even within the lifetime of one individual. Thus, only a rough estimate of shell growth rate is reasonable for this study: based on the 30 mm/year estimate provided by Ortega and Sutherland (1992) and carbon and oxygen isotope data presented by Surge et al. (2001), *C. virginica* growth rate in this study can be estimated at a few mm/month. This means that each ~1.5 cm^2 piece approximately represents a few months of growth. For each shell, three pieces of this size were crushed and homogenized collectively into a fine powder using an agate mortar and pestle. Homogenization of three separate pieces from each shell served to reduce the impact of seasonal variation while avoiding processing the entire shell, which could lead to detrital contamination of the Li fraction. Following the procedure of Dellinger et al. (2018), around 100 mg of homogenized powder from each oyster shell were subjected to a room-temperature ammonium acetate leach to reduce contamination from exchangeable ions, including isotopically light Li that is abundant in clay minerals (Dellinger et al., 2018; Pogge von Strandmann et al., 2020). To complete the leach, 1.5 mL of 1 N ammonium acetate were added to the samples before shaking

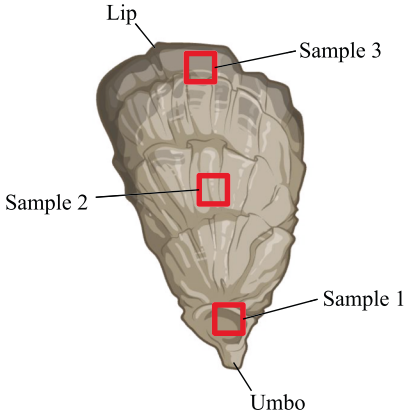

Fig. 2. Diagram of the left valve of an oyster shell. Squares show the three approximate sampling locations. Created in BioRender. Schaffer, A. (2026) https://BioRender.com/eeg9mqv.

for 30 min. Then, a rinsing process in which 3 mL Milli-Q H_2O were added to the samples before shaking for 10 min and then centrifuging for 10 min was repeated three times (with removal of the H_2O from the samples after each repetition).

The powder was then digested in 36 mL of 0.05 N HCl overnight to achieve 90% dissolution. We aimed to dissolve 90%, rather than 100%, of each powdered shell sample because full dissolution would increase the likelihood of clays embedded in the shell structure dissolving into the solution, as was suggested by Dellinger et al. (2018).

2.3. Li purification

Ion-exchange chromatography was used to isolate Li from the samples. Following methods described by James and Palmer (2000) and Dellinger et al. (2018), the samples (1–10 ng Li for shells and 100 ng Li for estuary water) were eluted with 0.5 N HCl through Savillex PFA columns (inner diameter of 6.4 mm) filled to a height of 12.5 cm (~4 mL) with Biorad AG50WX-12, 200–400 mesh resin. The isolated Li fraction was collected at 12–26 mL elution volume into Savillex PFA vials. Column yields for Li purification were consistently estimated at 98–102% based on analyses of geostandards. The purified samples were then evaporated to dryness (hot plate at 95°C), reacted with 1 mL H_2O_2 to decompose any organic matter, and redissolved in 2% HNO_3 in preparation for mass spectrometer analyses. All reagents used were high purity, either double distilled in-house or purchased (*e.g.*, Fisher "Optima" grade).

2.4. Li isotope analyses

Li isotope ratios were measured on a Nu Sapphire MC-ICP-MS in GAIA Lab (Geoscience Applications of Isotopic Analysis) at Duke University. Solutions at a concentration of 2.5–10 ppb Li were administered to the Sapphire via a microFAST Isotope2 (ESI) syringe injection system connected to an Apex Ω HF desolvating nebulizer (Liu et al., 2023), attaining a sensitivity of ~0.8 V/ppb. The instrument was operated in the high-energy (no collision-reaction cell) mode at low mass resolution. Each sample was bracketed with measurements of the IRMM-016 Li_2CO_3 standard. A single analysis consisted of 50 cycles of 4 s each; sample solutions were analyzed 1–3 times depending on Li content. All δ^7Li values are reported relative to the L-SVEC Li_2CO_3 standard using the calculation $\delta^7Li_{L\text{-}SVEC} = \delta^7Li_{IRMM\text{-}016} - 0.14‰$ (Brand et al., 2014).

The reproducibility of isotopic analyses was evaluated following published approaches (John and Adkins, 2010; Kipp et al., 2025; see Supplementary Material). The standard error of individual analyses was found to match the theoretical limits from Johnson noise and counting statistics (Fig. 3a). Replicate analyses of sample solutions yielded error-normalized deviates (END's) with standard deviations of 3.37 and 5.87 for water and shell analyses, respectively (Fig. 3b, c). This means that individual analyses under-represent the full analytical uncertainty. To be most conservative, the external reproducibility (2σ) is estimated as ±0.8‰ for water samples and ±3.6‰ for oyster shells based on replicate sample preparations and analyses. We note that this larger uncertainty derives from sample heterogeneity and/or variable Li contamination, not analytical conditions. In further support of analytical precision and accuracy, three samples of IAPSO seawater were measured and showed δ^7Li values of 30.2‰, 30.1‰, and 30.1‰, close to the established homogenous seawater value of 31.0‰ (Millot et al., 2004) and in agreement with other published values in the GeoReM database at 31.2‰ (Jochum et al., 2005).

2.5. Element ratio analyses

A 10 mL aliquot of each of the oyster shell digests used for Li isotope purification and analysis was used to measure Li/Ca, Mg/Ca, Sr/Ca, and Li/Mg ratios in the shells. Prior to measurement, the samples were diluted to an estimated uniform Ca concentration of 40 ppm to bring the samples within element concentration ranges optimal for ICP-MS analysis. The Li, Sr, Mg, and Ca analyses were then carried out on a ThermoFisher X-Series II ICP-MS at Duke University for samples and standards using collision cell mode (7% H_2/He at 4.5 mL/minute). To assess the accuracy and precision of the measured oyster shell elemental ratios, three $CaCO_3$ standards were analyzed along with samples and at equal spacing throughout the sample-analysis sequence: (1) Jcp-1, ~90% digested in 0.05 N HCl, similar to oyster samples, (2) Jcp-1, fully digested in 0.1 N HNO_3, and (3) Bahaman Pleistocene limestone standard PE-3, fully digested in 0.1 N HNO_3. Resultant Li/Ca (μmol mol^{-1}), Mg/Ca (mmol mol^{-1}), and Sr/Ca (mmol mol^{-1}) ratios, respectively, for the $CaCO_3$ standards were as follows: Jcp-1 (90% digestion), 6.38 ± 0.12, 4.26 ± 0.01, 8.96 ± 0.07; Jcp-1 (full digestion), 6.91 ± 0.13, 4.22 ± 0.02, 8.96 ± 0.02; PE-3 (full digestion), 7.02 ± 0.07, 8.46 ± 0.03, 7.86 ± 0.06 (all uncertainties are 2SE, n = 3). The measured element/Ca ratios are comparable to previously published values for Jcp-1 (Hathorne et al., 2013; Chen S. et al., 2023; Kipp et al., 2024) and PE-3 (Dwyer et al., 2002). Li/Ca, Mg/Ca, and Sr/Ca ratios in the water samples from the estuarine sampling sites were also determined under the same analytical conditions with the X-Series II, calibrated using the NIST water standard 1643f after diluting the samples to the working concentration range of 1643f.

2.6. Oxygen and carbon isotope analyses

Stable isotope analyses ($\delta^{18}O$, $\delta^{13}C$) were generated from powdered carbonate in the Paleo^3 Isotope Lab at North Carolina State University (NCSU). Analyses run at NCSU were carried out on a Nu Perspective IS Mass Spectrometer with a NuCarb Autosampler. Samples and standards (~200–500 μg) were digested at 70°C with orthophosphoric acid (ρ = 1.97 g/ml) in a NuCarb automated carbonate device, and the CO_2 released from the reaction was cryogenically purified using a series of

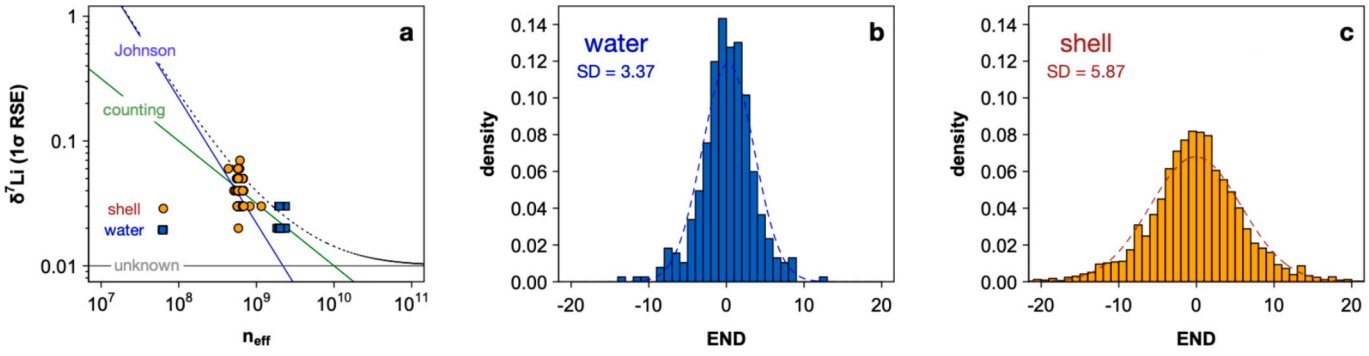

Fig. 3. Assessment of internal and intermediate analytical precision. Individual analyses follow predicted limits on precision imposed by Johnson noise and counting statistics. Replicate analyses show error-normalized deviates (END's) with SD > 1, reflecting greater dispersion of values than predicted by internal error alone.

cold fingers. Purified CO_2 was passed into a Nu Perspective IS Mass Spectrometer, which is set to measure *m/z* ratios for masses 44 to 49, via a dual inlet. All samples were analyzed against solid standards calibrated versus Vienna Peedee Belemnite (VPDB) for $\delta^{18}O$ and $\delta^{13}C$, and carbonate standards were analyzed using the same procedure utilized on sample replicates and were included in every run. The carbonate standards used include international standards NBS-18 and IAEA-603, and internal standard C64. Data were reduced using Easotope (John and Bowen, 2016), and long-term analytical uncertainty was maintained at < 0.1‰ for $\delta^{13}C$ and < 0.2‰ for $\delta^{18}O$.

3. Results

3.1. Salinity gradient

Salinity varies throughout the year and across the local estuary system, as demonstrated by continuous measurements from two monitoring stations (Fig. 4). In November 2024, salinity at the eight sampling sites ranged from 12.2 to 29.8 ppt. Between November 2024 and August 2025, salinity at the sites increased by an average of 8.6 ppt, exhibiting a new range of 24.4 to 36.2 ppt. Two-point average salinity between November 2024 and August 2025 ranges from 20.9 to 33.0 ppt. These values are taken to represent the average annual salinities in which the oysters lived and are used in subsequent isotope and element ratio analyses (see Section 4.1 for evaluation of the limitations of this two-point average method).

3.2. Lithium isotopes

Samples containing possible clay contamination (denoted by Al/Ca > 0.5 mmol mol^{-1}; see Section 4.3) were excluded from Li isotope analyses. For non-contaminated samples, δ^7Li_{shell} ranges from +23.0 to +38.9‰ with an average of +32.2 ± 1.4‰ (2SE, n = 35), within the range of data published for low-Mg calcite mollusks (Dellinger et al., 2018). δ^7Li_{water} values are less variable, ranging from +29.5 to +30.6‰ with an average of +30.2 ± 0.3‰ (2SE, n = 8) (Fig. 5a). In both oyster shell and estuary water samples, there is no significant relationship between δ^7Li and salinity (adj. $r^2 = -0.02$, $p = 0.55$ for oysters; adj. $r^2 = 0.01$, $p = 0.33$ for water). All water samples fall close to the global seawater value of +31‰ (Millot et al., 2004) (Fig. 5a). $\Delta^7Li_{shell\text{-}water}$ ($\delta^7Li_{shell} - \delta^7Li_{water}$), which ranges from −7.5 to 8.9‰, exhibits no correlation with salinity (adj. $r^2 = -0.02$, $p = 0.66$), and averages at +1.9 ± 1.5‰ (2SE, n = 35), showing that many of the shells are enriched in ^7Li relative to the water in which they grew (Fig. 5b).

3.3. Element ratios

$(Sr/Ca)_{shell}$ values range from 0.9 to 1.5 mmol mol^{-1} with an average of 1.2 ± 0.1 mmol mol^{-1} (2SE, n = 49), consistent with bivalve calcite data in the literature (*e.g.*, Klein et al., 1996; Dellinger et al., 2018) (Fig. 6). $(Sr/Ca)_{shell}$ displays a weak negative correlation with salinity (adj. $r^2 = 0.36$, $p < 0.001$). $(Sr/Ca)_{water}$, with a range of 7.6 to 8.0 mmol mol^{-1} and an average of 7.7 ± 0.1 mmol mol^{-1} (2SE, n = 8), correlates positively with salinity (adj. $r^2 = 0.46$, $p = 0.04$). $\Delta(Sr/Ca)_{shell\text{-}water}$ ($(Sr/Ca)_{shell} - (Sr/Ca)_{water}$), with a range of −6.9 to −6.1 mmol mol^{-1} and an average of −6.5 ± 0.1 mmol mol^{-1} (2SE, n = 49), exhibits a strong negative correlation with salinity (adj. $r^2 = 0.65$, $p < 0.001$) (Fig. 6). $(Li/Ca)_{shell}$ shows a range of 14.9 to 66.0 μmol mol^{-1} with an average of 24.8 ± 2.9 μmol mol^{-1} (2SE, n = 49), consistent with Li/Ca data published by Dellinger et al. (2018) for calcite mollusks, and exhibits a weak positive correlation with salinity (adj. $r^2 = 0.12$, $p = 0.01$) (Fig. 6). $(Li/Ca)_{water}$ shows a weak positive correlation with salinity (adj. $r^2 = 0.37$, $p = 0.09$) and has a range of 2240 to 2510 μmol mol^{-1} (one outlier at 6930 μmol mol^{-1} not included in analyses) with an average of 2340 ± 60 μmol mol^{-1} (2SE, n = 7). $\Delta(Li/Ca)_{shell\text{-}water}$, which has a range of −2490 to −2210 μmol mol^{-1} (excluding samples from site with outlier $(Li/Ca)_{water}$ value) and an average of –2320 ± 20 μmol mol^{-1} (2SE, n = 43), displays a negative correlation with salinity (adj. $r^2 = 0.45$, $p < 0.001$) (Fig. 6). $(Mg/Ca)_{shell}$ values range from 7.7 to 15.3 mmol mol^{-1} with an average of 10.8 ± 0.5 mmol mol^{-1} (2SE, n = 49), in agreement with

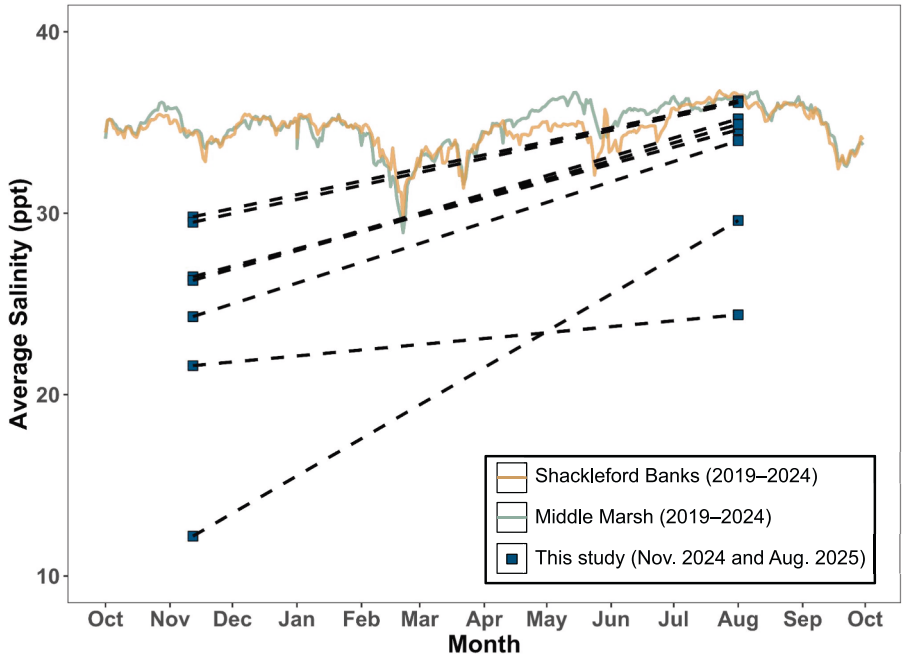

Fig. 4. Salinity time series and point samples. Brown and green lines track historic average daily salinity from March 2019 to September 2024 at two National Park Service monitoring stations close to the highest-salinity sampling sites (see *Fig. 1*). Blue squares represent point salinity values measured in November 2024 (date of oyster collection) and August 2025, with measurements taken at the same sampling site connected by a black dashed line. Note that the point samples were both taken after the window of continuous salinity data shown in the figure. Two-point average salinity between the two sampling dates was used for each sampling site in geochemical analyses. National Park Service data were acquired from NPS Aquarius web portal (https://irma.nps.gov/aqwebportal/).

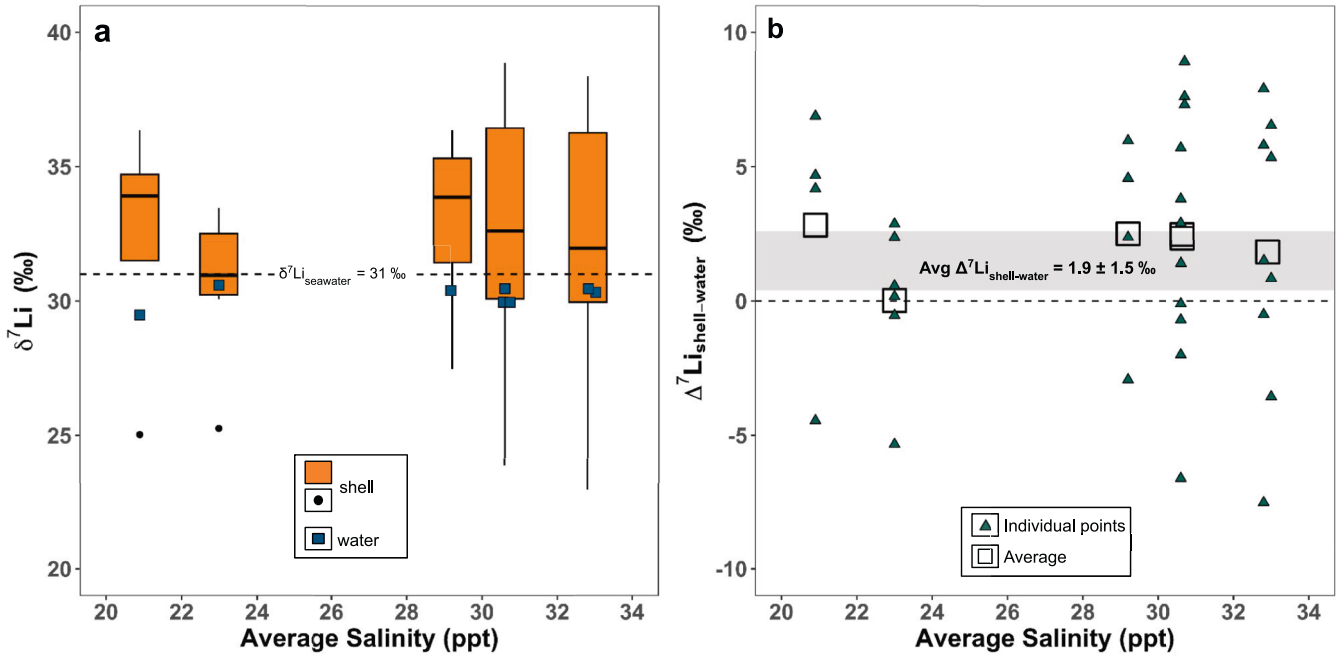

Fig. 5. (a) $\delta^7Li_{L\text{-}SVEC}$ in oyster and estuary water samples as a function of salinity. Oyster samples are grouped by sampling site. Sites with a < 2 ppt salinity difference are grouped together as one in this figure (both panels) but are analyzed statistically as separate sites. The black points denote shell outliers. The black dotted line shows $\delta^7Li_{seawater}$ = 31‰ (Millot et al., 2004). (b) $\Delta^7Li_{shell\text{-}water}$ as a function of salinity, where $\Delta^7Li_{shell\text{-}water} = \delta^7Li_{shell} - \delta^7Li_{water}$. The green triangles denote individual oysters, while the black squares denote average $\Delta^7Li_{shell\text{-}water}$ at each site. The grey shaded bar shows the average $\Delta^7Li_{shell\text{-}water}$ across all sampling sites: +1.9 ± 1.5‰ (2SE, n = 35).

previously published data for bivalve shell calcite (*e.g.*, Freitas et al., 2006; Dellinger et al., 2018). No correlation between $(Mg/Ca)_{shell}$ and salinity is observed (adj. $r^2 = -0.01$, $p = 0.53$). $(Mg/Ca)_{water}$ has a range of 4580 to 4800 mmol mol^{-1} with an average of 4690 ± 50 mmol mol^{-1} (2SE, n = 8) and shows a positive correlation with salinity (adj. r^2 = 0.55, $p = 0.02$). $\Delta(Mg/Ca)_{shell\text{-}water}$ ranges from −4790 to −4370 mmol mol^{-1} with an average of –4670 ± 20 mmol mol^{-1} (2SE, n = 49). A weak negative correlation is observed between $\Delta(Mg/Ca)_{shell\text{-}water}$ and salinity (adj. $r^2 = 0.31$, $p < 0.001$) (Fig. 6). $(Li/Mg)_{shell}$ ranges from 1.1 to 7.4 mmol mol^{-1} with an average of 2.4 ± 0.4 mmol mol^{-1} (2SE, n = 49), $(Li/Mg)_{water}$ ranges from 0.5 to 1.5 mmol mol^{-1} with an average of 0.6 ± 0.2 mmol mol^{-1} (2SE, n = 8), and $\Delta(Li/Mg)_{shell\text{-}water}$ ranges from −0.3 to 6.8 mmol mol^{-1} with an average of 1.8 ± 0.4 mmol mol^{-1} (2SE, n = 49). $(Li/Mg)_{shell}$ displays a weak positive correlation with salinity (adj. r^2 = 0.10, $p = 0.01$), while no correlation with salinity is observed for $(Li/Mg)_{water}$ (adj. $r^2 = -0.13$, $p = 0.68$) and $\Delta(Li/Mg)_{shell\text{-}water}$ (adj. r^2 = 0.06, $p = 0.05$) (Fig. 6). δ^7Li_{shell} shows no correlation with $(Li/Ca)_{shell}$ (adj. $r^2 = -0.02$, $p = 0.50$) (Fig. 7a) and $(Mg/Ca)_{shell}$ (adj. $r^2 = 0.07$, p = 0.06) (Fig. 7b).

3.4. Oxygen and Carbon Isotopes

$\delta^{18}O_{shell}$ ranges from −2.4 to + 0.5‰ (n = 49) and exhibits a positive correlation with salinity (adj. $r^2 = 0.54$, $p < 0.001$) (Fig. 8a). $\delta^{13}C_{shell}$ ranges from −5.2 to −0.9‰ (n = 49) and exhibits a strong positive correlation with salinity (adj. $r^2 = 0.77$, $p < 0.001$) (Fig. 8b). As salinity approaches seawater values (approximately 35 ppt), $\delta^{18}O_{shell}$ approaches the Vienna Standard Mean Ocean Water (VSMOW) value of $\delta^{18}O_{VSMOW}$ = 0‰ (Craig, 1961) (Fig. 8a). As salinity decreases towards 20.9 ppt, $\delta^{18}O_{shell}$ decreases in the direction of the regional freshwater end-member value (salinity ≈ 0 ppt) of $\delta^{18}O_{freshwater}$ = −4.3‰ from Hatteras, NC (Kendall and Coplen, 2001), demonstrating mixing of seawater and freshwater $\delta^{18}O$ reservoirs. $(Sr/Ca)_{shell}$ exhibits a weak negative correlation with $\delta^{18}O_{shell}$ (adj. $r^2 = 0.29$, $p < 0.001$) (Fig. 9).

4. Discussion

4.1. Establishing a salinity gradient

Oyster and water samples were collected from an estuary in North Carolina to encompass a wide range of salinities (Fig. 1). In addition to varying spatially, salinity varies temporally on daily, seasonal, and annual scales in estuarine environments (Fig. 4). Oysters grow their shells year-round, although at higher rates during the summer-fall rainy season (Surge et al., 2001). The oyster and water samples analyzed in this study were collected in November 2024, raising the question: to what extent do these point measurements represent the average annual salinity at each site?

To address this concern and estimate seasonal salinity variation in the estuary, salinity was measured at each of the eight sampling sites for a second time in August 2025. Furthermore, continuous, year-round salinity data from 2019 to 2024 were collected from two National Park Service monitoring stations (Shackleford Banks and Middle Marsh) within the target estuary system. The monitoring stations are located close to the estuary mouth and therefore are expected to represent the high salinity end-member of the sampling sites, which extend inland from the estuary mouth (Fig. 1). The sampling site closest to the estuary mouth exhibited a salinity of 29.5 ppt in November 2024 and 36.1 ppt in August 2025. These point measurements bookend the annual average salinity of 34.8 ppt calculated from the monitoring station data, suggesting important seasonal variation. Supporting this conclusion is the wide range of salinities seen throughout the year at the monitoring stations in Fig. 4 and our finding that salinity at the sampling sites increased by an average of 8.6 ppt between November 2024 and August 2025. Therefore, we suggest that a two-point average taken between November 2024 and August 2025 at each sampling site is the best possible representation of annual average salinity at the sampling sites in the absence of continuous, year-round salinity data at these locations.

To evaluate this interpretation, we turn to the two closest monitoring

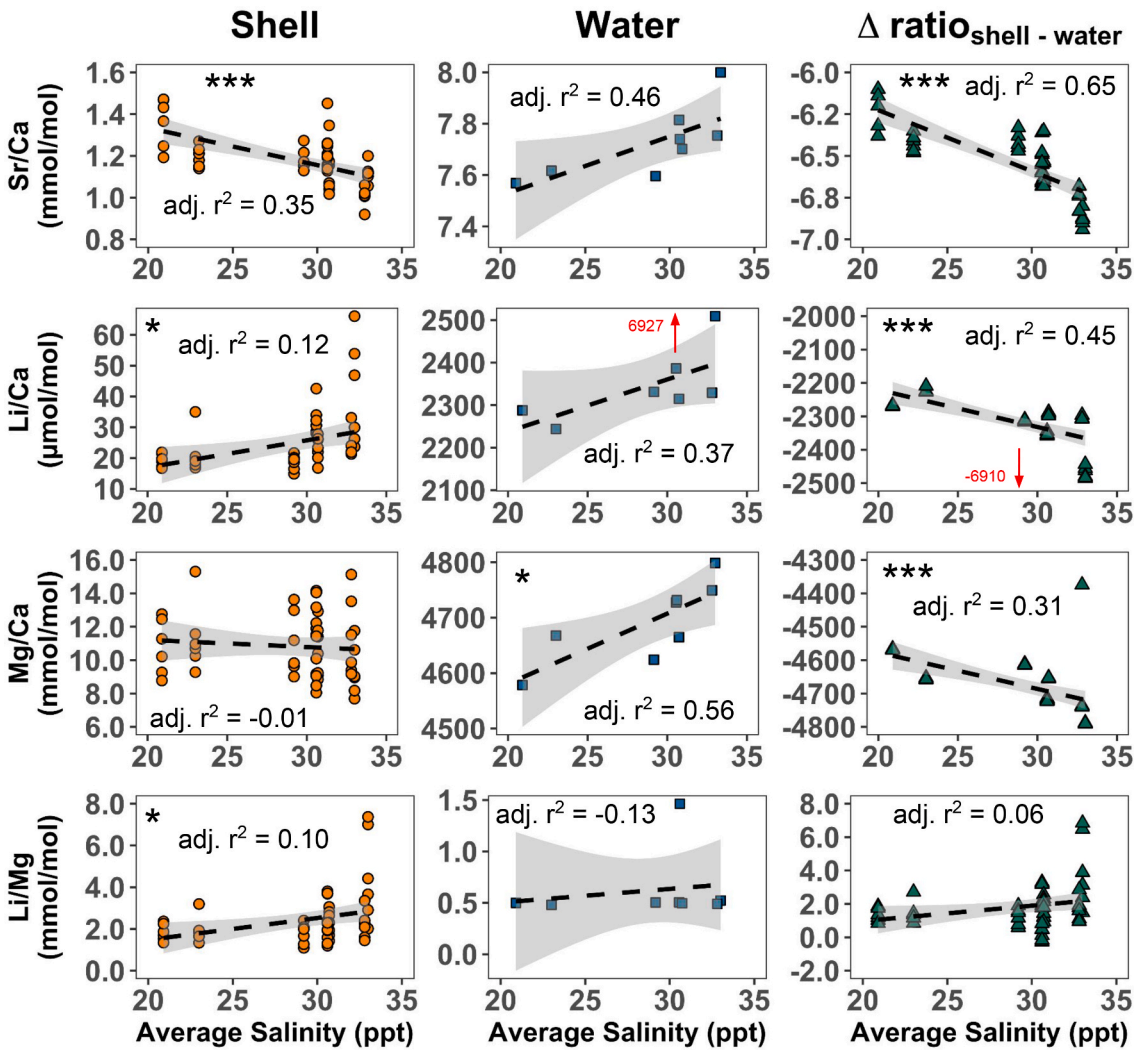

Fig. 6. Element ratios as a function of salinity in shell samples (left column) and water samples (middle column). The right column shows $\Delta(\text{ratio})_{\text{shell-water}} = (\text{ratio})_{\text{shell}} - (\text{ratio})_{\text{water}}$, where each shell sample is paired with the corresponding water sample taken from the site of shell collection. The black dashed line in each panel represents a linear approximation line with standard error as the grey shaded area. Red arrows in the middle and right panels of the Li/Ca row denote outlier values removed from analyses due to anomalously high [Li] concentration at one sampling site (one outlier in the middle panel, six outliers in the right panel resulting from calculations using the outlier $(\text{Li/Ca})_{\text{water}}$ value shown in the middle panel). Asterisks denote significance based on p-value: *** = < 0.001, ** = < 0.01, * = < 0.05.

stations from which continuous, year-long salinity data are available. The multi-year two-point average salinity between August (2019–2024) and November (2019–2023) is 35.1 ppt and 35.3 ppt at Shackleford Banks and Middle Marsh respectively, while the multi-year annual average salinity at the stations calculated using continuous, year-round data (2020–2023, the years that have year-round salinity measurements) is 34.7 ppt and 34.9 ppt. This suggests that the two-point average taken between August and November slightly overrepresents warmer, higher-salinity months and therefore is not a perfect representation of annual average salinity. If this inaccuracy were to result in an erroneous ordering of the sampling sites with respect to salinity, then subsequent analyses of the relationships between geochemical ratios and salinity using these data would be invalid. However, we note that the two-point average method produces the same small (0.2 ppt) difference between Middle Marsh and Shackleford Banks that is apparent in the true annual averages. We interpret this to indicate that, while deriving a quantitative proxy equation using the two-point average salinity data would prove erroneous, qualitatively assessing the sensitivity of δ^7Li and other geochemical ratios to salinity using this data is still reasonable. Thus, we have elected to use the two-point average salinities at the sampling sites between November 2024 and August 2025 for isotope and element ratio analyses while remaining cautious of the limitations of this method.

We also measured δ^{18}O in the oyster shell samples to determine how temperature and salinity influence the geochemical record at the sampling sites. δ^{18}O is an established temperature paleo-proxy in inorganic and organic carbonates (McCrea, 1950; Epstein et al., 1951), including bivalve shells (*e.g.*, Killingley and Berger, 1979; Wefer and Berger, 1991; Andrus and Crowe, 2000; Surge et al., 2001; Ullmann et al., 2010; Bougeois et al., 2016). If temperature were to differ substantially among the sampling sites in this study, we would expect $\delta^{18}O_{\text{shell}}$ to deviate from the line generated by typical mixing between the seawater end-member $\delta^{18}O_{\text{VSMOW}} = 0‰$ (Craig, 1961) and the local freshwater end-member $\delta^{18}O_{\text{freshwater}} = -4.3‰$ (Kendall and Coplen, 2001) (Fig. 8a). The $\delta^{18}O_{\text{shell}}$ values measured in this study closely track mixing between these reservoirs and do not deviate significantly from the mixing line (Fig. 8a). We take this to indicate that salinity, not temperature, is the primary control on variation among sampling sites in $\delta^{18}O_{\text{shell}}$ and other temperature-sensitive geochemical ratios measured in this study. We note that this is an indirect inference, as continuous temperature data at each sampling site are not available. However, if the $\delta^{18}O_{\text{shell}}$ variations observed in our data were in fact driven by temperature, they would imply a 7–10°C increase (McCrea, 1950; Epstein et al., 1951; Brand

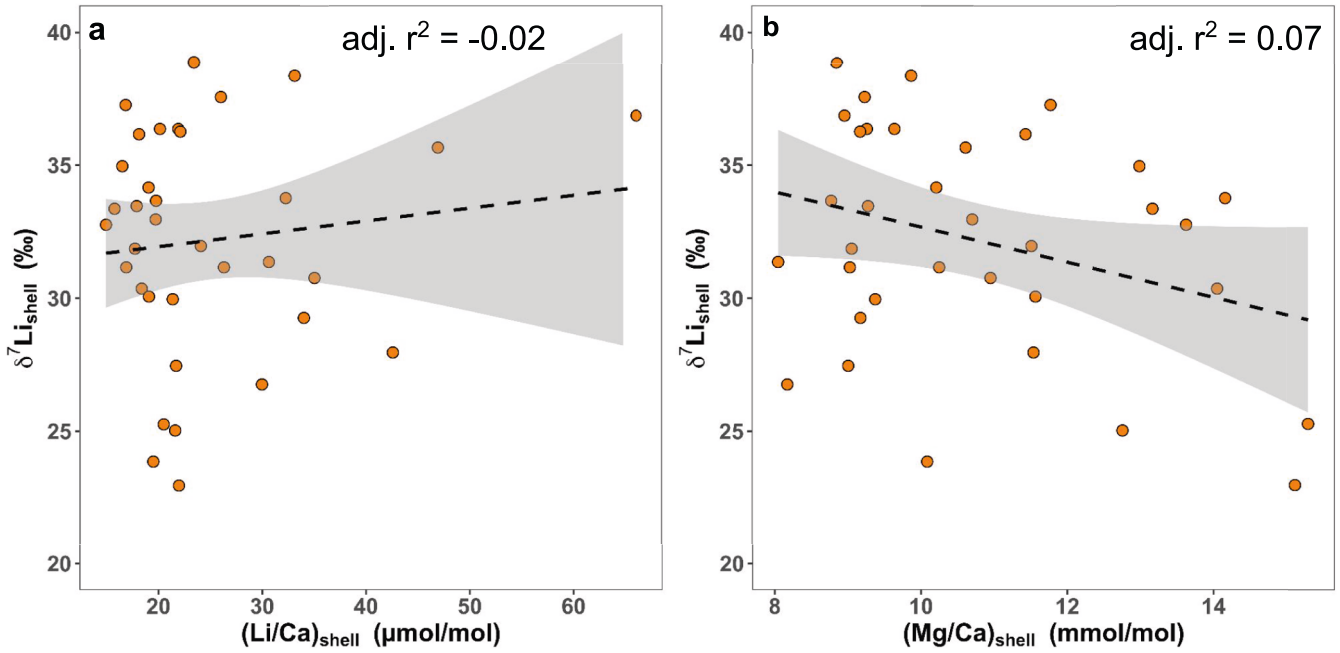

Fig. 7. δ^7Li_{shell} as a function of (a) $(Li/Ca)_{shell}$ and (b) $(Mg/Ca)_{shell}$. The black dashed line in each panel represents a linear approximation line with standard error as the grey shaded area. Both correlations are not significant ($p > 0.05$).

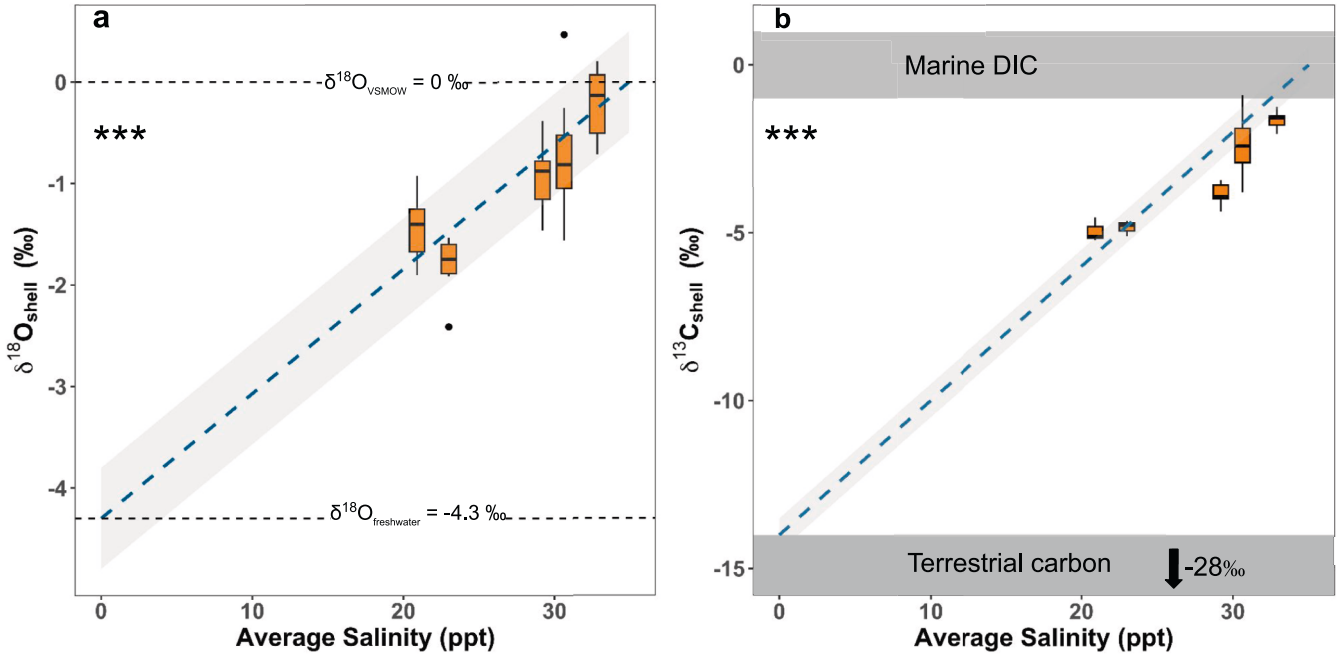

Fig. 8. (a) $\delta^{18}O_{shell}$ and (b) $\delta^{13}C_{shell}$ vs. salinity. In (a), the black dashed line at $\delta^{18}O = 0‰$ is the VSMOW value (Craig, 1961) and the black dashed line at $\delta^{18}O = -4.3‰$ is the freshwater end-member value measured near Hatteras, NC (Kendall and Coplen, 2001). The blue dashed line represents two-component mixing between seawater (salinity ≈ 35 ppt, $\delta^{18}O = 0‰$) and freshwater (salinity ≈ 0 ppt, $\delta^{18}O = -4.3‰$) end-members. In (b), the shaded box at $\delta^{13}C = -1‰$ to $\delta^{13}C = 1‰$ represents marine dissolved inorganic carbon (DIC), and the shaded box at $\delta^{13}C = -28‰$ (denoted by black arrow) to $\delta^{13}C = -14‰$ represents terrestrial carbon (organic carbon: C3 plants at −28‰ and C4 plants at −14‰) (O'Leary, 1988). The blue dashed line represents two-component mixing between these seawater (marine) and freshwater (terrestrial) end-members. Asterisks denote significance based on p-value: *** = < 0.001, ** = < 0.01, * = < 0.05.

et al., 2013) from the highest to lowest salinity samples, which seems unlikely given that all sites fall within a radius of several km (Fig. 1).

We furthermore measured $\delta^{13}C$, which is similarly sensitive to both salinity and temperature (*e.g.*, Surge et al., 2001). Our $\delta^{13}C_{shell}$ data also ostensibly track mixing between marine and terrestrial reservoirs (Fig. 8b), establishing $\delta^{13}C$ as a possible salinity proxy in *C. virginica*, as is posited by Surge et al. (2001). We acknowledge that $\delta^{13}C$ trends are less specific to salinity than $\delta^{18}O$ trends, but in Fig. 8b we show that the inferred freshwater end-member of our data fits within plausible composition of terrestrial organic carbon (O'Leary, 1988). Additionally,

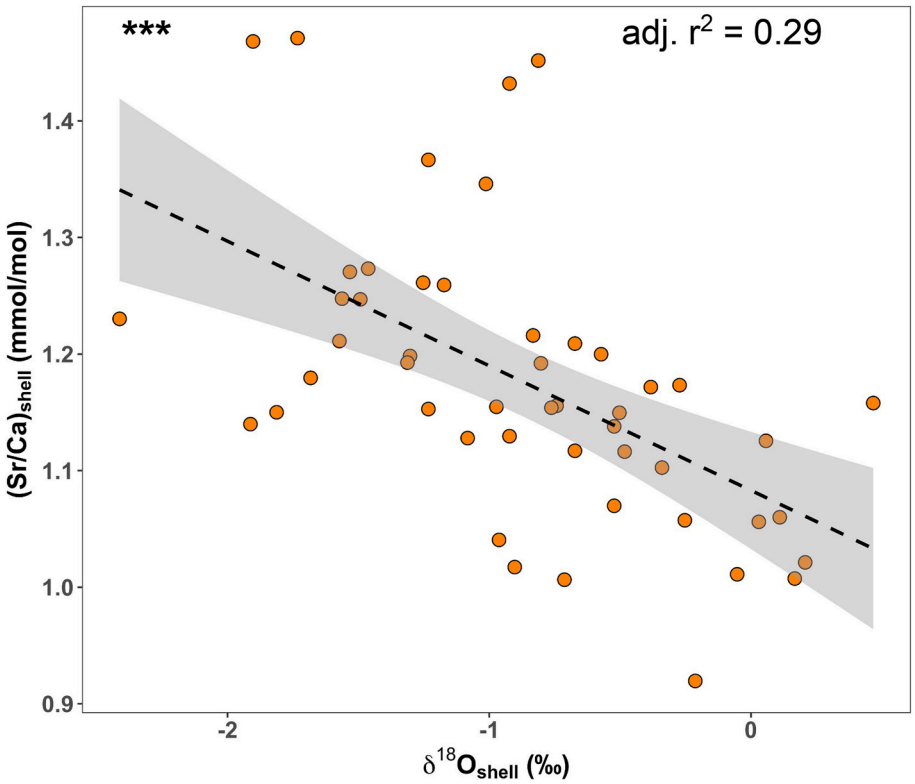

Fig. 9. $(Sr/Ca)_{shell}$ vs. $\delta^{18}O_{shell}$. The black dashed line represents a linear approximation line with standard error as the grey shaded area. Asterisks denote significance based on p-value: *** = < 0.001, ** = < 0.01, * = < 0.05.

if the $\delta^{13}C$ data were instead governed by the same hypothetical temperature gradient (~10°C) that would be required to explain the $\delta^{18}O$ values, they would show a much smaller trend (~1‰) than is observed (~4‰) (Craig, 1953). In sum, we interpret the $\delta^{18}O$ and $\delta^{13}C$ data as substantiating our sampling transect as capturing a salinity gradient, allowing us to now evaluate salinity effects on trace element ratios in oyster calcite.

4.2. Relationships of salinity and trace element ratios

We measured element ratios including Sr/Ca, Li/Ca, Mg/Ca, and Li/Mg in oyster shell and water samples across a salinity gradient to understand how environmental and vital effects influence shell composition. We turn first to Sr/Ca, which has been used as a temperature proxy in calcifying taxa including scleractinian corals (Beck et al., 1992; Gagan et al., 1998; Haase-Schramm et al., 2003; Cohen et al., 2006; Gaetani and Cohen, 2006; Fowell et al., 2016), sclerosponges (Haase-Schramm et al., 2003), foraminifera (Rathburn and De Deckker, 1997; Russell et al., 2004; Mortyn et al., 2005; Dissard et al., 2010), and bivalves (Freitas et al., 2006; Brosset et al., 2023). We observe a weak negative correlation between $(Sr/Ca)_{shell}$ and $\delta^{18}O_{shell}$ (adj. $r^2 = 0.29$, $p < 0.001$) (Fig. 9). Since we have interpreted $\delta^{18}O_{shell}$ in this study to be a proxy for salinity (Fig. 8a) and suggested that our sampling transect reflects no appreciable temperature gradient (see Section 4.1), we predict that $(Sr/Ca)_{shell}$ may also be sensitive to salinity, and we indeed observe a weak negative correlation between these two variables (adj. $r^2 = 0.36$, $p < 0.001$; Fig. 6). Interestingly, this contrasts with a positive correlation observed between $(Sr/Ca)_{water}$ and salinity (adj. $r^2 = 0.46$, $p = 0.04$), suggesting that Sr incorporation in oyster calcite does not strictly follow trends in estuary water Sr concentration. Rather, $(Sr/Ca)_{shell}$ may be determined by tight abiotic controls on Sr partitioning into the carbonate mineral (Mucci and Morse, 1983; Gabitov and Watson, 2006; Tang et al., 2008) and biological processes modulating the flux of Sr across membranes within the organism prior to shell precipitation (*e.g.*, Klein et al., 1996). Cohen et al. (2006) highlighted that the temperature dependence of Sr/Ca in scleractinian coral aragonite is much stronger than in inorganic aragonite, possibly due to seasonal differences in coral precipitation efficiency. Furthermore, growth rate seems to influence Sr/Ca in corals (de Villiers et al., 1995), brachiopods (Ullmann et al., 2017), and mollusks (Purton et al., 1999), and Klein et al. (1996) linked mantle metabolic rate to Sr/Ca in the calcite shell of the blue mussel *Mytilus edulis*. If, as the preceding evidence suggests, Sr/Ca in calcifying organisms is controlled by abiotic and biological regulation, we would expect to see similar trends in other Ca-substituting elements, bringing us to our discussion of Li/Ca and Mg/Ca.

Many studies have found that Li/Ca and Mg/Ca are sensitive to temperature in inorganic and biogenic carbonates (Delaney et al., 1989; Marriott et al., 2004a, 2004b; Butler et al., 2015; Rollion-Bard and Blamart, 2015; Dellinger et al., 2018). However, just as in Sr/Ca, temperature trends in biogenic aragonite Li/Ca and Mg/Ca are superimposed by inorganic precipitation effects and biological effects (Case et al., 2010; Gabitov et al., 2011; Montagna et al., 2014; Rollion-Bard and Blamart, 2015; Marchitto et al., 2018). While these Li/Ca and Mg/Ca controls are less well-studied in biogenic calcite, Thébault and Chauvaud (2013) found a strong correlation between Li/Ca and calcification rate in the calcite shell of the king scallop *Pecten maximus*, and Dellinger et al. (2018) observed a positive correlation between Li/Ca and Mg/Ca in several calcite and aragonite taxa, indicating that these ratios are influenced by similar abiotic and/or biological processes. Dellinger et al. (2018) also found distinct Li/Ca values among calcifying taxa, even within low-Mg calcite and aragonite groups, suggesting a biological influence on the incorporation of Li into biogenic carbonates. We observe in our data that $(Li/Ca)_{shell}$ and $(Mg/Ca)_{shell}$ are substantially lower than $(Li/Ca)_{water}$ and $(Mg/Ca)_{water}$ throughout the sampling transect, with an average $\Delta(Li/Ca)_{shell\text{-}water}$ of –2320 ± 20 μmol mol^{-1} (after excluding outlier $\Delta(Li/Ca)_{shell\text{-}water}$ values derived from an outlier $(Li/Ca)_{water}$ value) and an average $\Delta(Mg/Ca)_{shell\text{-}water}$ of –4670 ± 20 mmol mol^{-1} (Fig. 6). It is important to note that this may reflect abiotic,

rather than biological, regulation: studies have observed discrimination against incorporation of Li (Marriott et al., 2004a, 2004b; Füger et al., 2019, 2022) and Mg (Mucci and Morse, 1983; Hartley and Mucci, 1996; Burton and Walter, 1987; Howson et al., 1987; Mucci, 1987; Oomori et al., 1987; Huang and Fairchild, 2001; Mavromatis et al., 2013) in inorganic calcite. In agreement with previous work (Bryan and Marchitto, 2008; Case et al., 2010; Planchon et al., 2013; Montagna et al., 2014; Dellinger et al., 2018), we suggest that noise in our Li/Ca_{shell} and Mg/Ca_{shell} (Fig. 6) data reflect the influence of both abiotic and biological factors.

Biological fractionation can potentially be corrected by normalizing Li/Ca to Mg/Ca, isolating temperature effects in the Li/Mg ratio (Bryan and Marchitto, 2008; Case et al., 2010; Montagna et al., 2014). Indeed, Li/Mg has been shown to be largely insensitive to vital effects and exhibits a negative correlation with temperature in biogenic aragonite (Bryan and Marchitto, 2008; Case et al., 2010; Hathorne et al., 2013; Raddatz et al., 2013; Montagna et al., 2014; Fowell et al., 2016; Dellinger et al., 2018; Marchitto et al., 2018; Cuny-Guirriec et al., 2019; Ross et al., 2019; Stewart et al., 2020), high-Mg calcite (Anagnostou et al., 2019; Stewart et al., 2020), and low-Mg calcite (Chen D. et al., 2023). Therefore, we would expect any substantial temperature differences among our sampling sites to be reflected in our Li/Mg data. We observe that $(Li/Mg)_{shell}$ remains relatively constant across our sampling transect and exhibits only a weak positive correlation with salinity (adj. $r^2 = 0.10$, $p = 0.01$), indicating that, as we suggested in Section 4.1, our sampling transect exhibits no appreciable temperature trend and instead captures a salinity gradient. Montagna et al. (2014) and Case et al. (2010) found no correlation between Li/Mg and salinity in aragonite scleractinian corals over salinity ranges of 34.7 to 38.7 ppt and 34.0 to 36.5 ppt, respectively. We tentatively extend this to an estuarine range of 20.9 to 33.0 ppt and to low-Mg calcite oyster shells.

We postulate two speculative explanations (not mutually exclusive) for the relative constancy of $(Li/Mg)_{shell}$ despite mixing of freshwater and seawater reservoirs. First, this could be an artifact of Li and Mg both existing in much higher concentrations in seawater relative to freshwater (Millero, 2016), such that the Li/Mg ratio is constant down to very low salinity. Second, Li and Mg could be influenced by one or more similar physiological processes (*e.g.*, Dellinger et al., 2018), such that any measurable changes in these processes that correlate with salinity are corrected when Li/Ca is normalized by Mg/Ca. We discuss possible physiological processes that could influence oyster shell composition in Section 4.5.

4.3. Evaluation of clay contamination and diagenesis

We measured δ^7Li in modern oyster shell and estuary water samples to determine whether δ^7Li_{shell} is a faithful paleo-water archive that can be used to track ancient silicate rock weathering. A consequence of silicate rock weathering is the formation of clay minerals that preferentially incorporate ^6Li from solution ($\delta^7Li_{clay} - \delta^7Li_{growth\ solution} = -24$ to -14‰, Pogge von Strandmann et al. 2020). Clays can be entrenched within shell layers, possibly contributing contaminant Li with highly fractionated δ^7Li values. Thus, before analyzing δ^7Li_{shell} data, it is crucial to identify and remove δ^7Li_{shell} values that may have been contaminated by isotopically light clay particles. We have modeled clay contamination in carbonates following Pogge von Strandmann et al. (2013), starting with the mass balance equation

$$\delta^7Li_{shell}[Li]_{shell} = \delta^7Li_{clay}[Li]_{clay} + \delta^7Li_{carb}[Li]_{carb} \quad (1)$$

where $[Li]_{clay}$ denotes the moles of Li derived from clay contamination and $[Li]_{carb}$ denotes the moles of Li in pristine shell calcite. $[Li]_{shell}$ denotes the shells measured in this study, which presumably contain the total moles of Li derived from both clay contamination and pristine shell-hosted Li: $[Li]_{shell} = [Li]_{clay} + [Li]_{carb}$. Assuming that the aluminum (Al) fraction in the shell, denoted by $[Al]_{shell}$, is derived primarily from the clay and $[Ca]_{shell}$ is derived primarily from the pristine shell, we can infer that $[Li]_{clay} = \left(\frac{Al}{Ca}\right)_{shell}\left(\frac{Li}{Al}\right)_{clay}[Ca]_{shell}$ and $[Li]_{carb} = \left(\frac{Li}{Ca}\right)_{carb}[Ca]_{shell}$. Thus, the equation can be rewritten as

$$\delta^7Li_{shell}\left(\left(\frac{Al}{Ca}\right)_{shell}\left(\frac{Li}{Al}\right)_{clay}[Ca]_{shell} + \left(\frac{Li}{Ca}\right)_{carb}[Ca]_{shell}\right) = \delta^7Li_{clay}\left(\frac{Al}{Ca}\right)_{shell}\left(\frac{Li}{Al}\right)_{clay}[Ca]_{shell} + \delta^7Li_{carb}\left(\frac{Li}{Ca}\right)_{carb}[Ca]_{shell} \quad (2)$$

Factoring out $[Ca]_{shell}$ and isolating δ^7Li_{shell}, we arrive at:

$$\delta^7Li_{shell} = \frac{\delta^7Li_{clay}\left(\frac{Al}{Ca}\right)_{shell}\left(\frac{Li}{Al}\right)_{clay} + \delta^7Li_{carb}\left(\frac{Li}{Ca}\right)_{carb}}{\left(\frac{Al}{Ca}\right)_{shell}\left(\frac{Li}{Al}\right)_{clay} + \left(\frac{Li}{Ca}\right)_{carb}} \quad (3)$$

We have assumed the end-members of clay Li isotope composition to be 24‰ and 14‰ lower than δ^7Li_{carb} (in this model $\delta^7Li_{carb} = 31$‰, the seawater value generally tracked by biogenic carbonates), such that $\delta^7Li_{clay\_low} = 31‰ - 24‰ = 7‰$ and $\delta^7Li_{clay\_high} = 31‰ - 14‰ = 17‰$ (values from Pogge von Strandmann et al. 2020). We note that detrital Li contamination could potentially also carry a crustal isotopic composition (~0‰), which would have an even stronger isotopic impact. However, since we do not see significant occurrence of low δ^7Li_{shell} values at high Al/Ca in our data, we do not further consider this possibility.

We adopted $\left(\frac{Li}{Al}\right)_{clay} = 0.001$ mmol mol^{-1} (Pogge von Strandmann et al., 2013) and $\left(\frac{Li}{Ca}\right)_{carb} = 24.8$ μmol mol^{-1} (this study). Using our measured $(Al/Ca)_{shell}$ values and adopting the conservative $\delta^7Li_{clay} = \delta^7Li_{clay\_low} = 7$‰, we calculated that $(Al/Ca)_{shell} > 0.5$ mmol mol^{-1} from clay contamination would result in a negative perturbation in δ^7Li_{shell} of > 0.5‰ from the seawater value of 31‰. Thus, we have removed samples with $(Al/Ca)_{shell} > 0.5$ mmol mol^{-1} (Fig. 10) from Li isotope analyses, resulting in rejection of nine out of 44 samples. This screening reduces the likelihood that δ^7Li_{shell} has been influenced on a resolvable scale (> 0.5‰) by contamination from isotopically light clays, enabling us to more confidently assess environmental and physiological drivers of observed δ^7Li patterns. We note that our observed Li isotope trends and conclusions are not significantly affected by this screening.

In addition to exogenous clay contamination, we consider diagenetic alteration of carbonate-hosted Li isotope signatures. Diagenesis has been found to influence δ^7Li and other geochemical signatures in modern and ancient carbonates (Patterson and Walter, 1994; Ullmann and Korte, 2015; Dellinger et al., 2018; Fantle et al., 2020; Murphy et al., 2022). The low-Mg calcite oyster shells measured in this study show $(Mn/Ca)_{shell}$ values ranging from 0.0 to 0.1 mmol mol^{-1}, well below the proposed upper limit for Mesozoic low-Mg calcite bivalves of 0.5 mmol mol^{-1} (Korte et al., 2009; Korte and Hesselbo, 2011), above which diagenesis could be an appreciable factor. This is consistent with the fresh nature of the samples collected. Furthermore, diagenesis is known to result in depletion of strontium in low-Mg calcite, and $(Sr/Ca)_{shell}$ values in this study range from 0.9 to 1.5 mmol mol^{-1}, above the lower limit of 0.5 mmol mol^{-1} for pristine Mesozoic bivalves, below which diagenesis should be considered (Korte and Hesselbo, 2011). Interestingly, $(Fe/Ca)_{shell}$ values range from 0.4 to 0.9 mmol mol^{-1}, above the proposed upper limit of 0.5 mmol mol^{-1}, (Wierzbowski and Joachimski, 2007), possibly signaling diagenetic alteration. However, the samples with the highest $(Fe/Ca)_{shell}$ values also display $(Al/Ca)_{shell}$ values > 0.5 mmol mol^{-1}, suggesting that detrital contamination, not diagenesis, is responsible for positive $(Fe/Ca)_{shell}$ anomalies in our data. After screening out samples with $(Al/Ca)_{shell} > 0.5$ mmol mol^{-1} following the

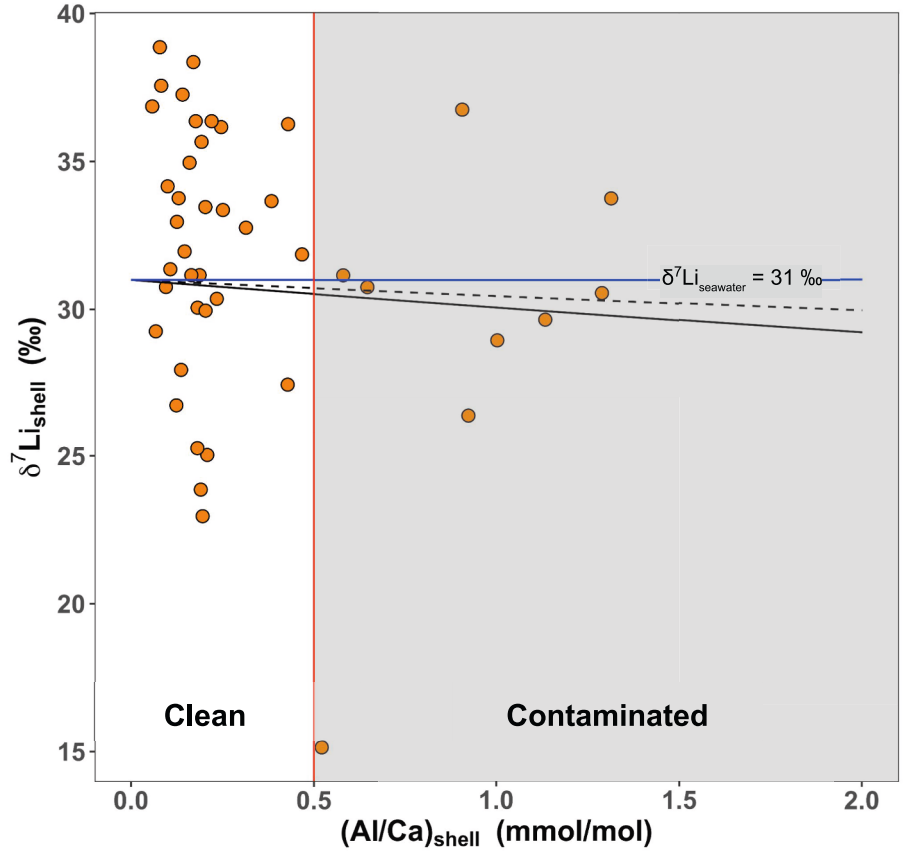

Fig. 10. δ^7Li_{shell} vs. $(Al/Ca)_{shell}$. Any shell samples with $(Al/Ca)_{shell} > 0.5$ mmol mol^{-1} (right of the red vertical line) are considered to be potentially contaminated by isotopically light clays and have been removed from δ^7Li analyses. The blue horizontal line represents $\delta^7Li_{seawater} = 31‰$. The black solid line shows δ^7Li_{shell} as a function of $(Al/Ca)_{shell}$ according to Eq. (3), where $\delta^7Li_{clay} = \delta^7Li_{clay\_low} = 7‰$. This end-member represents maximum ^7Li depletion in clays and was used to calculate a conservative contamination cutoff value of $(Al/Ca)_{shell} = 0.5$ mmol mol^{-1} (if this entire $[Al]_{shell}$ fraction is from contaminant clay particles, the resultant δ^7Li_{shell} perturbation would be −0.5‰). The black dashed line represents δ^7Li_{shell} as a function of $(Al/Ca)_{shell}$ according to Eq. (3), where $\delta^7Li_{clay} = \delta^7Li_{clay\_high} = 17‰$. This end-member represents minimum ^7Li depletion in clays and would yield a more lenient contamination cutoff value of $(Al/Ca)_{shell} = 0.9$ mmol mol^{-1}. The conservative $(Al/Ca)_{shell}$ cutoff value (0.5 mmol mol^{-1}, black solid line) was used to screen for contamination in this study. When testing the more lenient contamination cutoff value, no significant changes in isotopic trends were observed.

procedure described in the previous paragraph, $(Fe/Ca)_{shell}$ values of the cleaned data range from 0.4 to 0.6 mmol mol^{-1}, much closer to 0.5 mmol mol^{-1} upper limit for biogenic carbonate. Altogether, we take this to indicate minimal influence of diagenesis on the geochemical measurements presented in this study.

4.4. Lithium isotope ratios across a salinity gradient

Our δ^7Li_{shell} and δ^7Li_{water} data exhibit no correlation with salinity (adj. $r^2 = -0.02$, $p = 0.55$ for oysters; adj. $r^2 = 0.01$, $p = 0.33$ for water) (Fig. 5a), suggesting that δ^7Li is not sensitive to changes associated with estuary mixing. This trend is consistent with precipitation experiments conducted by Marriott et al. (2004b) showing that salinity variations do not influence δ^7Li in inorganic calcite or aragonite. A key limitation to the proxy potential of δ^7Li in oyster shells is its wide intra-site range, which in this study averages at 9.2‰. Thus, while measuring several shells may produce an average δ^7Li_{shell} value relatively close to δ^7Li_{water}, individual shell values vary widely above and below δ^7Li_{water} (Fig. 5a, b). A fair bit of this variance can likely be explained by the small amount of Li recovered from our samples, which limits analytical precision, as well as lingering small-magnitude impacts of detrital Li contamination. The remainder may derive from inconsistent "vital effects" (see Section 4.5). We conservatively suggest that studies using oyster shell Li isotopes to elucidate the Li isotope composition of past water bear in mind this variability and aim to improve precision by undertaking larger or replicate samples.

Additional estuarine parameters that were not measured in this study may covary with salinity in our transect and must be considered. Carbonate saturation state (Ω) is known to increase between fresh and saline end-members in estuarine environments (*e.g.*, Reisdorph and Mathis, 2014; Hu et al., 2022; Shi and Zhai, 2025). Day et al. (2021) showed that the Li isotope fractionation factor of precipitated calcite is not influenced by changes in carbonate saturation state, leading us to suggest that the probable trend of increasing carbonate saturation state with increasing salinity in our transect does not exert an appreciable influence on δ^7Li_{shell}. Estuarine salinity also often shows a positive relationship with dissolved inorganic carbon (DIC) (*e.g.*, Oliveira et al., 2017; Yan et al., 2020) and pH, although the relationship with pH stabilizes in salinities higher than ~15 ppt (*e.g.*, Mook and Koene, 1975; Mosley et al., 2010; Omarjee et al., 2021). In light of these observations, we speculate that DIC and pH may increase with salinity in our transect. Since we observe no relationship between δ^7Li_{shell} and salinity, we hypothesize that δ^7Li_{shell} is also insensitive to DIC and pH in this study, consistent with findings of no correlation between δ^7Li and either DIC or pH in cultured low-Mg calcite benthic foraminifera (genus *Amphistegina*) tests (Charrieau et al., 2023) and experimentally precipitated inorganic calcite and aragonite (Hite et al., 2025). However, we note that Vigier et al. (2015) observed a positive correlation between δ^7Li and DIC in *Amphistegina* tests, and Seyedali et al. (2021) and Füger et al. (2022) observed increasing $\Delta^7Li_{carb\text{-}solution}$ (analog to $\Delta^7Li_{shell\text{-}water}$ in this

study) with increasing pH in inorganic calcite. We therefore suggest that our hypotheses regarding the insensitivity of δ^7Li_{shell} to DIC and pH may not be applicable beyond the shells measured in this study, and we encourage future experimental work directly examining the influence of DIC and pH on δ^7Li in bivalve calcite to resolve this matter.

4.5. Revisiting environmental and vital effects on Li isotopes in biogenic carbonates

Looking in finer detail, we note that, on average, δ^7Li_{shell} is +1.9 ± 1.5‰ higher than δ^7Li_{water} (Fig. 5b) after screening for potentially clay-contaminated samples (see Section 4.3). Presumably, accounting for this offset in fossil shells may allow for calculation of δ^7Li of ancient water. However, δ^7Li ranges are highly variable among calcifying taxa and carbonate polymorphs, with biogenic aragonite and calcite occupying wide δ^7Li ranges of +15 to +24‰ and +25 to +40‰, respectively (Dellinger et al., 2018) (Fig. 11a). Biogenic aragonite δ^7Li is generally lower than seawater δ^7Li yet higher than inorganic aragonite δ^7Li, while biogenic low-Mg calcite δ^7Li varies from lower to higher than both seawater and inorganic calcite δ^7Li with an apparent taxon dependence (Fig. 11a). As discussed in Section 4.3, some of this variance may be explained by limits on the current analytical precision of Li isotope measurements and a small amount of detrital Li contamination. Another potential contributing factor is inorganic Li isotope fractionation during shell precipitation. Hite et al. (2025) precipitated inorganic aragonite and calcite to find an average $\Delta^7Li_{carb\text{-}sol}$ in aragonite of –16.3 ± 0.5‰ and in calcite of –3.5 ± 0.3‰. Some studies have proposed an equilibrium fractionation effect where Li is more weakly coordinated in the carbonate mineral phase than in the solution phase, causing ^6Li to preferentially reside in the mineral phase (Marriott et al., 2004a, 2004b; Hite et al., 2025). However, increased growth rate has been shown to correlate with increased incorporation of Li (Füger et al. 2019) and decreased δ^7Li values (Day et al., 2021; Füger et al., 2022) in inorganic calcite – a signal of kinetic, rather than equilibrium, fractionation. In this kinetic model, enrichment of light isotopes in the carbonate phase relative to solution phase has been proposed to occur during desolvation of hydrated Li, where more weakly coordinated, isotopically lighter hydration spheres are desolvated faster and thus are preferentially incorporated into the precipitating $CaCO_3$ mineral, driving carbonate δ^7Li to lower values than growth solution δ^7Li (Hofmann et al., 2012; Füger et al., 2022).

Abiotic kinetic fractionation is likely responsible for some variation in δ^7Li of biogenic carbonates, but abiotic factors such as pH and carbonate growth rate would have to exhibit implausibly high variation among and within taxa and environments for abiotic fractionation alone to generate the wide range of δ^7Li values observed in this study and the existing literature (Fig. 11a). Furthermore, abiotic fractionation does not explain the significant deviations of biogenic δ^7Li from inorganic δ^7Li observed in both aragonite and calcite. We instead propose that a substantial amount of the δ^7Li variation observed in biogenic carbonates is generated by biological fractionation occurring during internal transmembrane transport of Li prior to shell precipitation, as was suggested by Dellinger et al. (2018). In this model, abiotic kinetic fractionation is not negated at the precipitation site; rather, it is imparted on an internal calcifying fluid that has already been pre-fractionated relative to seawater. We therefore now discuss speculative physiological mechanisms that could fractionate Li isotopes prior to shell precipitation.

In bivalves, ions first enter the organism through a continuous seawater current generated in the pallial cavity (Fig. 12). The incorporated seawater is passed over the gills for filter feeding, at which point it becomes known as the pallial fluid. Upon exiting the pallial fluid, ions pass through a thin membrane called the inner mantle epithelium (IME) to enter the hemolymph, analog for blood in the open circulatory system of bivalves (Eble and Scro, 1996; Planchon et al., 2013) (Fig. 12). From the hemolymph, some ions are incorporated into soft tissues, where they serve as nutrients or aid in other biological processes. Ions in the hemolymph may also be transported through the outer mantle epithelium (OME) into extrapallial cavities that reside between the mantle and the shell and contain the extrapallial fluid (EPF) from which the $CaCO_3$ shell precipitates (see Alvarez Caraveo et al., 2025; Planchon et al., 2013) (Fig. 12). This flux into the EPF (known as the calcifying fluid in non-molluscan taxa) is the primary source of ions for shell formation in bivalves. Physiological isotope fractionation of elements including Li, Mg, and Ca is thought to occur along the internal ion transport pathways shown in Fig. 12 (*e.g.*, Planchon et al., 2013; Dellinger et al., 2018; Alvarez Caraveo et al., 2025). To experimentally resolve the direction and strength of all possible Li isotope fractionations occurring along these pathways, Li isotopes in the EPF, OME, hemolymph, and soft tissues would have to be measured and compared. Unfortunately, the sensitivity of Li isotope measurements is currently too low to measure these Li-poor reservoirs. We therefore limit the scope of the following discussion to Li transport pathways directed into and out of the EPF, the closest internal reservoir to the shell.

Conditions inside the EPF are modified in various ways to make the calcification reaction ($Ca^{2+} + CO_3^{2-} \rightarrow CaCO_3$) more favorable. For example, calcification is driven forward by removal of ions (such as Mg^{2+}) that could inhibit carbonate precipitation by substituting for Ca^{2+} or occupying interstitial spaces in the carbonate crystal lattice (Berner, 1975; Zeebe and Sanyal, 2002; Bracco et al., 2012; Dellinger et al., 2018; Knight et al., 2023). While the fate of these removed ions is uncertain, Planchon et al. (2013) suggested that Mg^{2+} could be incorporated into soft tissues after being transported out of EPF, presumably by first crossing the OME into the hemolymph (Fig. 12). Several studies have proposed that passive and active ion removal from the EPF or calcifying fluid is responsible for significant vital effects in isotope and element ratios in biogenic carbonates (Klein et al., 1996; Zeebe and Sanyal, 2002; Bentov and Erez, 2006; Bentov et al., 2009; Ries, 2010; Planchon et al., 2013; Immenhauser et al., 2016; Dellinger et al., 2018; Marchitto et al., 2018). Other mechanisms of modifying EPF chemistry to favor calcification include elevation of pH (Erez, 2003; Bentov et al., 2009) and pumping of Ca into the EPF (Al-Horani et al., 2003; Böhm et al., 2006; Hippler et al., 2009; Ries, 2010; Marchitto et al., 2018), both of which have been proposed to impart isotopic fractionation on ions including Li and Ca (*e.g.*, Gussone et al., 2006; Hippler et al., 2013; Vigier et al., 2015). Mollusks are also thought to use a complex organic matrix to arrange nucleating crystals into ideal orientations for carbonate shell precipitation (Watabe and Wilbur, 1960; Ries, 2010), but resolving the behavior of Li isotopes within organic templates is beyond the scope of the current analytical sensitivity of Li isotope measurements. In the following paragraphs we evaluate the potential of transmembrane ion transport mechanisms to fractionate Li isotopes in the EPF and contribute to the large variations observed in the Li isotope composition of biogenic carbonates in this study and previous works (Fig. 11a). Since there are no known measurements of δ^7Li and Li/Ca in the internal reservoirs of the calcifying organisms being discussed, we have generated our hypotheses by drawing on the existing literature and stress that the following interpretations are speculative and lack direct experimental evidence.

A possible physiological process that could influence Li isotope fractionation in biogenic carbonates is the removal of Li from the EPF. Dellinger et al. (2018) proposed that Li in the EPF behaves similarly to Mg. In calcite, Mg^{2+} is easily adsorbed and incorporated into the crystal lattice as $MgCO_3$, which is substantially more soluble than $CaCO_3$ and thus reduces calcite growth (Berner, 1975; Lahann, 1978; Davis et al., 2000). Consequently, decreased [Mg^{2+}] in the EPF makes calcite precipitation more favorable (Ries, 2010; Immenhauser et al., 2016; Dellinger et al., 2018). Several studies have proposed that Mg is transported out of the EPF or calcifying fluid via channels or pumps (*e.g.*, Zeebe and Sanyal, 2002; Bentov and Erez, 2006; Ries, 2010; Immenhauser et al., 2016; Marchitto et al., 2018; Dellinger et al., 2018), and the existence of a Mg removal mechanism is consistent with observations of low Mg/Ca ratios in biogenic compared to inorganic carbonates (Ulrich et al.,

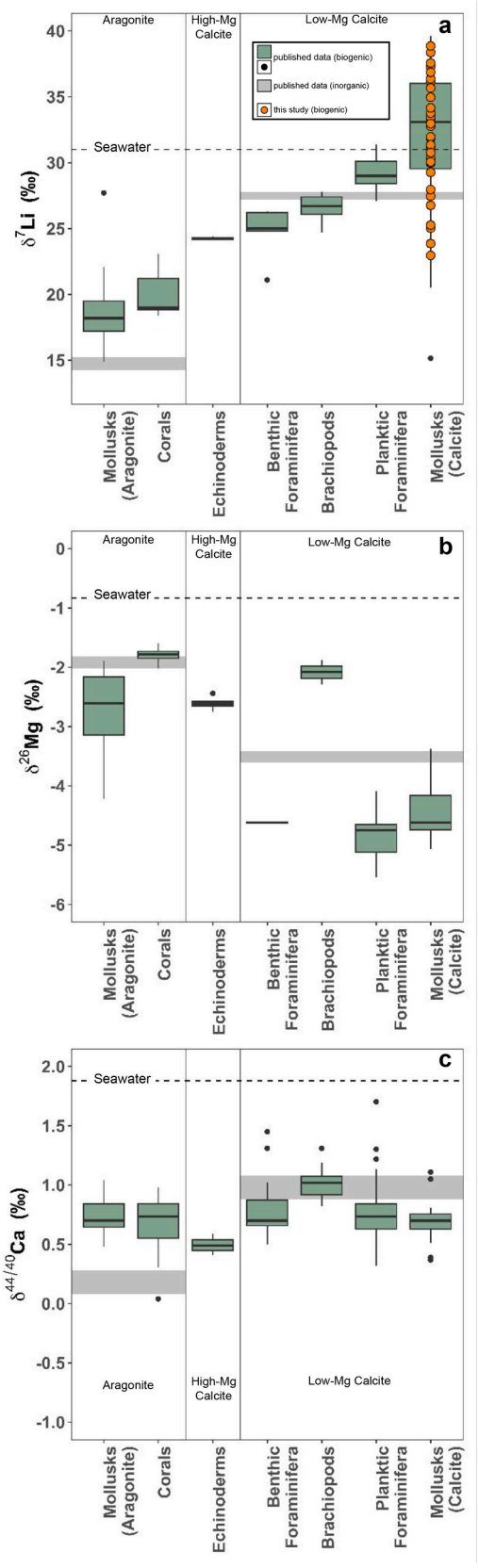

(caption on next column)

Fig. 11. (a) Adapted from Dellinger et al. (2018): δ^7Li of modern aragonite, high-Mg calcite, and low-Mg calcite taxa. All δ^7Li values are reported relative to the L-SVEC Li_2CO_3 standard. Data for aragonite mollusks are from Dellinger et al. (2018), corals from Marriott et al. (2004a) and Rollion-Bard et al. (2009), echinoderms from Dellinger et al. (2018), benthic foraminifera from Marriott et al. (2004b), brachiopods from Dellinger et al. (2018), planktic foraminifera from Hathorne and James (2006), and calcite mollusks from this study and Dellinger et al. (2018). Grey shaded bars show inorganic δ^7Li values of aragonite and low-Mg calcite. These values were calculated by adding the fractionation from growth solution, shown by Hite et al. (2025) to be –16.3 ± 0.5‰ (2SE, n = 23) for aragonite and –3.5 ± 0.3‰ (2SE, n = 25) for low-Mg calcite, to the seawater value of 31‰ (Millot et al., 2004). (b) δ^{26}Mg of modern aragonite, high-Mg calcite, and low-Mg calcite taxa relative to Dead Sea Metal Company (DSM3) standard. Data for biogenic carbonates were compiled by Saenger and Wang (2014), with data for aragonite mollusks from Planchon et al. (2013), Yoshimura et al. (2011), and Pogge von Strandmann (2008), corals from Wombacher et al. (2011), Yoshimura et al. (2011), Saenger et al. (2013), Hippler et al. (2009), and Planchon et al. (2013), echinoderms from Hippler et al. (2009) and Wombacher et al. (2011), brachiopods from Hippler et al. (2009) and Wombacher et al. (2011), planktic foraminifera from Pogge von Strandmann (2008) and Wombacher et al. (2011), and calcite mollusks from Hippler et al. (2009). Grey shaded bars show δ^{26}Mg of inorganic aragonite and inorganic calcite. These values were calculated by adding the fractionation from growth solution, which was shown to be –1.1 ± 0.1‰ (estimated range) for aragonite (Wang et al., 2013) and –2.7 ± 0.1‰ (estimated range) for low-Mg calcite (Li et al., 2012), to the seawater value of −0.8‰ (Pogge von Strandmann, 2008). (c) $\delta^{44/40}$Ca of modern aragonite, high-Mg calcite, and low-Mg calcite taxa relative to NIST SRM 915a standard. Data for aragonite mollusks are from Steuber and Buhl (2006) and Hippler et al. (2013), corals from Zhu and Macdougall (1998), Chang et al. (2004), Böhm et al. (2006), Blättler et al. (2012), Holmden et al. (2012), and Pretet et al. (2013), echinoderms from Skulan et al. (1997) and Blättler et al. (2012), benthic foraminifera from Skulan et al. (1997), Zhu and Macdougall (1998), and Gussone et al. (2016), brachiopods from Gussone et al. (2005), Steuber and Buhl (2006), Farkaš et al. (2007), and von Allmen (2010), planktic foraminifera from Zhu and Macdougall (1998), Gussone et al. (2003), Gussone et al. (2005), Heuser et al. (2005), Sime et al. (2005), Griffith et al. (2008), Kasemann et al. (2008), and Holmden et al. (2012), and calcite mollusks from Steuber and Buhl (2006), Heinemann et al. (2008), and Ullmann et al. (2013). Grey shaded bars show $\delta^{44/40}$Ca values of inorganic aragonite and inorganic calcite. These values were calculated by adding the fractionation from growth solution, which was shown to be –1.7 ± 0.1‰ (estimated range) for aragonite (Gussone et al., 2003, 2005) and –0.9 ± 0.1‰ (estimated range) for low-Mg calcite (Marriott et al., 2004a), to the seawater value of 1.88‰ (Hippler et al., 2013).

2021). Dellinger et al. (2018) hypothesized that a similar process could remove Li from the EPF; in particular, passive transport of Li through a channel directed out of the EPF (Fig. 12) could impart a kinetic isotope fractionation effect where ^{6}Li is preferentially removed from the EPF, resulting in an enrichment of ^{7}Li in the EPF that is recorded during carbonate precipitation.

The hypothesis that removal of Mg from the EPF is coincident with removal of ^{6}Li is indirectly supported by negative correlations between δ^7Li and Mg/Ca and between δ^7Li and Li/Ca in low-Mg calcite mollusks observed by Dellinger et al. (2018). However, in our oyster shell data, δ^7Li_{shell} shows no correlation with Li/Ca_{shell} (adj. $r^2 = -0.02$, $p = 0.50$) (Fig. 7a) and Mg/Ca_{shell} (adj. $r^2 = 0.07$, $p = 0.06$) (Fig. 7b), possibly indicating the influence of other biological or shell precipitation effects on Li isotope composition (see Marriott et al., 2004a, 2004b; Gabitov et al., 2011; Montagna et al., 2014; Rollion-Bard and Blamart, 2015; Day et al., 2021). Furthermore, a comparison of Li and Mg isotope data in the literature reveals that these two elements may behave less similarly during biological transport than previously thought (Fig. 11a, b). If passive transport of Li out of the EPF results in preferential removal of ^{6}Li, then the analog mechanism acting on Mg should preferentially remove the lighter Mg isotope (^{24}Mg), leaving the EPF enriched in the heavier ^{26}Mg isotope. We would therefore expect to see higher δ^{26}Mg values in biogenic carbonates than in inorganic carbonates. However, the opposite trend is observed in the literature: δ^{26}Mg values in biogenic

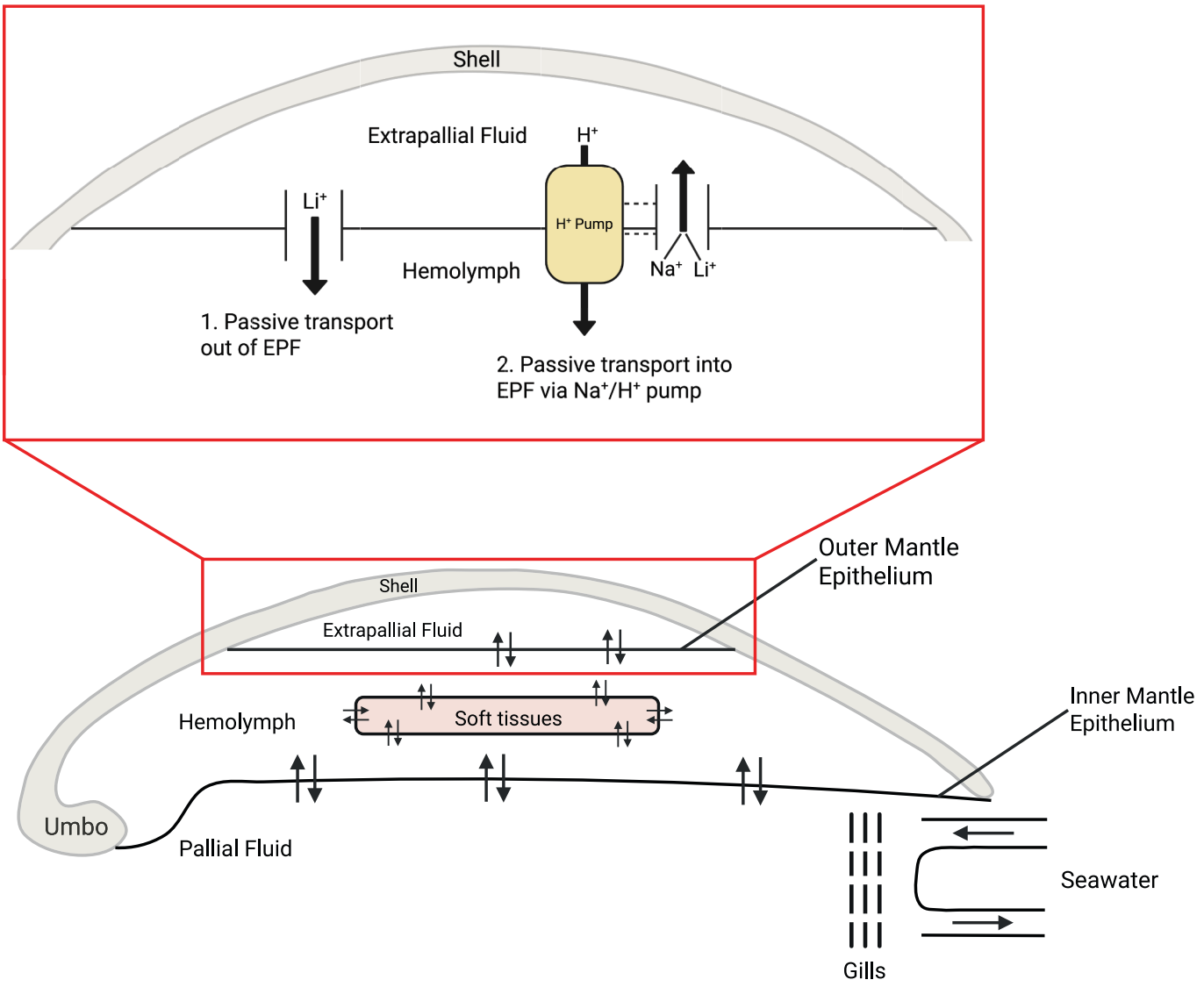

Fig. 12. Adapted from Alvarez Caraveo et al. (2025) and Planchon et al. (2013): Simplified illustration of ion transport through a bivalve. Ions enter through a seawater current passed over the gills and are then transported into multiple internal reservoirs, including the extrapallial fluid (EPF) from which some ions are taken up into the shell during calcification. The inset in red shows two tentatively proposed mechanisms of Li transport across the outer mantle epithelium, (1) out of and (2) into the EPF. Created in BioRender. Schaffer, A. (2026) https://BioRender.com/gp7bvjg, (inset) https://BioRender.com/kwto57y.

.

calcite and aragonite are mostly lower than in their inorganic counterparts (Fig. 11b) (save for the notable exceptions of brachiopods and corals), suggesting that possible enrichment of isotopically heavy Mg in the EPF resulting from passive Mg removal may be overprinted by one or more processes concentrating isotopically light Mg in the EPF.

Planchon et al. (2013), who observed lower δ^{26}Mg in the hemolymph than in the soft tissues of the manila clam *Ruditapes philippinarum*, suggested that transport of Mg from the hemolymph into the soft tissues could be facilitated by a transport protein with a large binding site that attaches to the hydrated form of Mg. This could generate an equilibrium fractionation effect where the more stable, more strongly coordinated Mg hydration spheres with heavier Mg isotopes are preferentially incorporated into the transport protein and shuttled into the soft tissues (Planchon et al., 2013). We speculate that a similar active transporter could preferentially pump isotopically heavy Mg out of the EPF, driving the EPF and consequently the shell toward lower δ^{26}Mg values, although such a mechanism has not been shown experimentally. Inclusion of Li in this transport pathway is unlikely because hydrated Mg has a substantially larger radius than hydrated Li (0.428 nm for Mg and 0.382 nm for Li) (Volkov et al., 1997). Ultimately, we suggest that Li and Mg are decoupled and transported (for the most part) independently between the EPF and the surrounding internal reservoirs. Even if ^{6}Li is indeed preferentially removed from the EPF through passive channels analogous to speculated Mg removal channels (Dellinger et al., 2018) (Fig. 12), as we tentatively proposed in the previous paragraphs, this mechanism alone does not explain the tendency of δ^{7}Li in some carbonate taxa to fall below inorganic values (indicating an EPF enriched in ^{6}Li) (Fig. 11a). We therefore now explore additional possible ion transport pathways that could concentrate light Li isotopes in the EPF.

One such pathway was proposed by Vigier et al. (2015), who cultured benthic foraminifera of the genus *Amphistegina* and found that decreased growth solution DIC was associated with decreased δ^{7}Li in the low-Mg calcite test. To explain this trend, they hypothesized that decreased DIC leads to decreased pH in the calcifying fluid, which in *Amphistegina* is contained within seawater vacuoles. This would warrant increased pumping of protons out of the calcifying fluid to raise pH, since elevated pH increases the rate of $CaCO_3$ formation. Vigier et al. (2015) suggested that the organism allows for passive diffusion of Na^{+}

into the seawater vacuoles to enable pumping of protons across a low-to-high concentration gradient out of the vacuoles into the surrounding cytosol. Li^+ could be moved into the vacuoles along with Na^+ due to the similar atomic properties of these two elements, possibly generating a kinetic fractionation effect where ^6Li is preferentially transported into the calcifying fluid (Vigier et al., 2015). We propose that a similar process could occur in bivalves (Fig. 12), although we note that mollusks are thought to elevate internal pH to a lesser extent than other calcifying groups (Ries, 2010). Enrichment of ^6Li in the EPF via an Na^+/H^+ pump could occur concurrently with passive transport of Li out the EPF (described in the previous paragraphs and shown in Fig. 12), resulting in a highly variable EPF composition dependent on the relative strengths of these mechanisms. For example, DIC and therefore the strength of the Na^+/H^+ pump could vary across environments, further complicating the Li isotope composition of the EPF (Vigier et al., 2015).

Additional clues about the behavior of Li and Li isotopes inside marine calcifying organisms may be found in Ca isotope trends in the literature. Ca, like Li, is isotopically heavier in biogenic aragonite than in inorganic aragonite (Fig. 11a, c). One possible cause of this offset is preferential active transport of heavier Ca isotopes into the EPF (Hippler et al., 2013). In this speculative model, Ca transport proteins in the OME would bind to hydrated Ca molecules, causing more strongly coordinated (and isotopically heavier) Ca to be preferentially transported into the EPF. In low-Mg calcite, however, $\delta^{44/40}Ca$ (denoted as such to avoid confusion with $\delta^{44/42}Ca$) ranges from higher to lower than the inorganic low-Mg calcite values, again resembling trends in δ^7Li (Fig. 11a, c). This suggests that isotopic fractionation during transport through the OME is also capable of enriching the EPF in light Ca isotopes. Studies have suggested that this fractionation could be induced by a Ca^{2+}-ATPase pump that transports dehydrated Ca^{2+} into the calcifying fluid (Cohen and McConnaughey, 2003; Gillikin et al., 2005). Dehydration of Ca at the protein binding site could allow for lighter Ca isotopes, which form more weakly coordinated hydration spheres and therefore dehydrate faster, to be preferentially transported into the calcifying fluid (Gussone et al., 2006). While resolving the causes of possibly different Ca transport mechanisms and consequently different $\delta^{44/40}Ca$ in the calcifying fluid between aragonite and calcite organisms is beyond the scope of this study, it is useful to note that calcite organisms maintain a lower relative Mg concentration in the calcifying fluid/EPF than is required for aragonite organisms; one speculative method of achieving this is increased transport of Ca into the calcifying fluid (Gussone et al., 2016), which could generate differential isotopic fractionation. Another potential mechanism is increased pumping of Mg out of the EPF in calcite organisms, which could be capable of removing some hydrated Ca in addition to hydrated Mg due to their similar hydrated radii (Volkov et al., 1997), but neither differential rates of Mg removal nor a coupling therein of Ca and Mg have been shown experimentally.

Involvement of Li in the above described Ca transport pathways would have to overcome the difference in hydrated radius between these two elements (0.412 nm for Ca and 0.382 for Li; Volkov et al., 1997), which is smaller than the difference in hydrated radius between Mg and Li but is not negligible, and/or the difference in surface charge between dehydrated Ca^{2+} and Li^+. In light of these challenges and a lack of experimental evidence for coupled Ca and Li transport, we suggest that Ca transport pathways are unlikely to cause significant fractionation of Li isotopes. However, Ca isotope systematics may still provide valuable insights to future work unraveling biological Li isotope fractionation in marine calcifying organisms.

In our discussion of Li isotope fractionation in bivalves, we have proposed preferential removal of light Li isotopes from the EPF via passive channels (Dellinger et al., 2018) and preferential transport of light Li isotopes into the EPF via an Na^+/H^+ pump (proposed for foraminifera by Vigier et al., 2015) (Fig. 12). These mechanisms do not explain the tendency of different marine calcifying taxa to exhibit distinct δ^7Li values (Fig. 11a). It is perhaps too early to resolve the causes of this trend, but future experimental studies measuring Li isotopes in internal reservoirs such as the EPF, hemolymph, and soft tissues could illuminate any taxon-dependence in Li transport pathways. Ultimately, we suggest that multiple pathways of biological fractionation acting in opposite directions generate large variability of δ^7Li in the EPF (Fig. 12). This variability is then preserved in the shell after being offset by a roughly constant abiotic kinetic fractionation effect at the precipitation site that shifts aragonite δ^7Li by –16.3 ± 0.5‰ and calcite δ^7Li by –3.5 ± 0.3‰ (Hite et al., 2025) relative to the pre-fractionated EPF. The wide range of δ^7Li values within and among taxa brings into question the viability of fossil carbonate δ^7Li as a recorder of past estuary water and seawater δ^7Li; thus, it is crucial to not only quantify deviations from water δ^7Li values in biogenic carbonates but also to understand the biological mechanisms driving these perturbations.

4.6. Conclusions

In this study we measured δ^7Li, element/Ca ratios, and $\delta^{18}O$ and $\delta^{13}C$ in low-Mg calcite eastern oyster shells from an estuarine environment. The $\delta^{18}O$ and $\delta^{13}C$ values demonstrate a clear trend with salinity, matching predicted values for mixing between freshwater and seawater end-members. We interpret this to substantiate our sampling transect as capturing a salinity gradient where temperature is not the primary control on variation in geochemical measurements, allowing us to analyze Li isotope ratios as they relate to salinity and estuary mixing. To this end, we observe no correlation between δ^7Li and salinity in shell and water samples, suggesting that δ^7Li is not a viable paleo-proxy for past salinity. This finding also shows that, at least within the range of 20.9 to 33.0 ppt sampled in this study, salinity is not a confounding factor when evaluating δ^7Li in oyster shells as a potential record of δ^7Li in past estuary water, which can be used to reconstruct past silicate weathering congruency (*e.g.*, Misra and Froelich, 2009; Pogge von Strandmann et al., 2017, 2020).

Upon further examination of our δ^7Li data, we notice an interesting trend: δ^7Li values in oyster shells are +1.9 ± 1.5‰ higher on average than the δ^7Li values of the water in which they grew, in contrast to precipitation experiments showing that δ^7Li values in inorganic carbonates are lower than growth solution values (Marriott et al., 2004a, 2004b; Hite et al., 2025). This indicates a strong vital effect. We discuss multiple possible mechanisms of physiological Li isotope fractionation, including passive transport of Li (preferentially ^6Li) out of the EPF and a Na^+/H^+ pump that transports Li (preferentially ^6Li) into the EPF. Our discussion of these mechanisms remains speculative; while our Li isotope data provide evidence for the presence of a vital effect on oyster shell δ^7Li, they do not constrain the mechanism driving this effect. We are not able to resolve the wide variation of δ^7Li within and among taxa seen in the literature, but we suggest that new studies could identify a widely variable EPF or calcifying fluid composition influenced by involvement of Li in multiple ion transport pathways whose relative strengths depend on environmental and biological factors. Calibrations of δ^7Li may only be applied across taxa and to fossil archives once taxonomic variations in Li isotope systematics are better understood, allowing for accurate, taxon-specific corrections for vital effects. We therefore encourage future work tracking fractionation of Li isotopes during ion transport in calcifying organisms, as understanding the vital effects on δ^7Li is crucial to developing this geochemical signature as a potential proxy for reconstructing past silicate weathering congruency.

CRediT authorship contribution statement

Alexandra M. Schaffer: Writing – original draft, Visualization, Methodology, Investigation, Data curation. **Gordon D.Z. Williams:** Writing – review & editing, Methodology, Investigation. **Gary S. Dwyer:** Writing – review & editing, Methodology, Investigation. **Ethan G. Hyland:** Writing – review & editing, Methodology, Investigation. **Juliet M. Wong:** Writing – review & editing, Methodology. **Joshua S. Osterberg:** Writing – review & editing, Methodology. **Thomas F. Schultz:**

Writing – review & editing, Methodology. **Michael A. Kipp:** Writing – review & editing, Supervision, Methodology, Funding acquisition.

Declaration of competing interest

The authors declare that they have no known competing financial interests or personal relationships that could have appeared to influence the work reported in this paper.

Acknowledgments

We thank Rosa Grigoryan for laboratory assistance. We thank Philip Pogge von Strandmann for editorial handling and Anthony Dosseto and two anonymous reviewers for helpful comments. This work was performed in part at the Duke University Shared Materials Instrumentation Facility (SMIF), a member of the North Carolina Research Triangle Nanotechnology Network (RTNN), which is supported by the National Science Foundation (award no. ECCS-2025064) as part of the National Nanotechnology Coordinated Infrastructure. AMS was supported by a SMIF Undergraduate User Program award. This work was also financially supported by an NSF CAREER grant (no. 2441483), ACS PRF grant (no. 67594 DNI2), and start-up funds (Duke University) to MAK.

Appendix A. Supplementary material

Supplementary material contains all geochemical data generated and compiled in this study. Supplementary material also includes an explanation of calculations performed to assess the reproducibility of the Li isotope analyses presented in this study (see Section 2.4).

Supplementary material to this article can be found online at https://doi.org/10.1016/j.gca.2026.06.025.

Data availability

All data are available through EarthChem Library at https://doi.org/10.60520/IEDA/114514.

References

Al-Horani, F.A., Al-Moghrabi, S.M., de Beer, D., 2003. The mechanism of calcification and its relation to photosynthesis and respiration in the scleractinian coral *Galaxea fascicularis*. Mar. Biol. 142, 419–426.

von Allmen, K., Nägler, T.F., Pettke, T., Hippler, D., Griesshaber, E., Logan, A., Eisenhauer, A., Samankassou, E., 2010. Stable isotope profiles (Ca, O, C) through modern brachiopod shells of *T. septentrionalis* and *G. vitreus*: Implications for calcium isotope paleo-ocean chemistry. Chem. Geol. 269, 210–219.

Alvarez, C.B., Guillermic, M., Downey-Wall, A., Cameron, L.P., Sutton, J.N., Higgins, J. A., Ries, J.B., Lotterhos, K., Eagle, R.A., 2025. Magnesium (Mg/Ca, δ^{26}Mg), boron (B/Ca, δ^{11}B), and calcium (Ca^{2+}) geochemistry of *Arctica islandica* and *Crassostrea virginica* extrapallial fluid and shell under ocean acidification. Biogeosciences 22, 2831–2851.

Anagnostou, E., Williams, B., Westfield, I., Foster, G.L., Ries, J.B., 2019. Calibration of the pH-δ^{11}B and temperature-Mg/Li proxies in the long-lived high-latitude crustose coralline red alga *Clathromorphum compactum* via controlled laboratory experiments. Geochim. Cosmochim. Acta 254, 142–155.

Andrus, C.F.T., Crowe, D.E., 2000. Geochemical analysis of *Crassostrea virginica* as a method to determine season of capture. J. Archaeol. Sci. 27, 33–42.

Beck, J.W., Edwards, R.L., Ito, E., Taylor, F.W., Recy, J., Rougerie, F., Joannot, P., Henin, C., 1992. Sea-surface temperature from coral skeletal strontium/calcium ratios. Science 257, 644–647.

Bentov, S., Brownlee, C., Erez, J., 2009. The role of seawater endocytosis in the biomineralization process in calcareous foraminifera. Proc. Natl. Acad. Sci. 106, 21500–21504.

Bentov, S., Erez, J., 2006. Impact of biomineralization processes on the Mg content of foraminiferal shells: a biological perspective. Geochem. Geophys. Geosyst. 7.

Berner, R.A., 1975. The role of magnesium in the crystal growth of calcite and aragonite from sea water. Geochim. Cosmochim. Acta 39, 489–504.

Blättler, C.L., Henderson, G.M., Jenkyns, H.C., 2012. Explaining the Phanerozoic Ca isotope history of seawater. Geology 40, 843–846.

Böhm, F., Gussone, N., Eisenhauer, A., Dullo, W.-C., Reynaud, S., Paytan, A., 2006. Calcium isotope fractionation in modern scleractinian corals. Geochim. Cosmochim. Acta 70, 4452–4462.

Bougeois, L., de Rafélis, M., Reichart, G.-J., de Nooijer, L.J., Dupont-Nivet, G., 2016. Mg/Ca in fossil oyster shells as palaeotemperature proxy, an example from the Palaeogene of Central Asia. Palaeogeogr. Palaeoclimatol. Palaeoecol. 441, 611–626.

Bracco, J.N., Grantham, M.C., Stack, A.G., 2012. Calcite growth rates as a function of aqueous calcium-to-carbonate ratio, saturation index, and inhibitor concentration: insight into the mechanism of reaction and poisoning by strontium. Cryst. Growth Des. 12, 3540–3548.

Brand, U., Azmy, K., Bitner, M.A., Logan, A., Zuschin, M., Came, R., Ruggiero, E., 2013. Oxygen isotopes and $MgCO_3$ in brachiopod calcite and a new paleotemperature equation. Chem. Geol. 359, 23–31.

Brand, W.A., Coplen, T.B., Vogl, J., Rosner, M., Prohaska, T., 2014. Assessment of international reference materials for isotope-ratio analysis (IUPAC Technical Report). Pure Appl. Chem. 86, 425–467.

Broecker, W.S., Peng, T.-H., 1982. Tracers in the Sea. Eldigio Press.

Brosset, C., Höche, N., Witbaard, R., Nishida, K., Shirai, K., Mertz-Kraus, R., Schöne, B.R., 2023. Sr/Ca in shells of laboratory-grown bivalves (Arctica islandica) serves as a proxy for water temperature – implications for (paleo)environmental research? Front. Mar. Sci. 10.

Bryan, S.P., Marchitto, T.M., 2008. Mg/Ca–temperature proxy in benthic foraminifera: new calibrations from the Florida Straits and a hypothesis regarding Mg/Li. Paleoceanography 23.

Burton, E.A., Walter, L.M., 1987. Relative precipitation rates of aragonite and Mg calcite from seawater: temperature or carbonate ion control? Geology 15, 111–114.

Butler, S., Bailey, T.R., Lear, C.H., Curry, G.B., Cherns, L., McDonald, I., 2015. The Mg/Ca–temperature relationship in brachiopod shells: Calibrating a potential palaeoseasonality proxy. Chem. Geol. 397, 106–117.

Case, D.H., Robinson, L.F., Auro, M.E., Gagnon, A.C., 2010. Environmental and biological controls on Mg and Li in deep-sea scleractinian corals. Earth Planet. Sci. Lett. 300, 215–225.

Chan, L.H., Edmond, J.M., Thompson, G., Gillis, K., 1992. Lithium isotopic composition of submarine basalts: implications for the lithium cycle in the oceans. Earth Planet. Sci. Lett. 108, 151–160.

Chan, L.-H., Edmond, J.M., 1988. Variation of lithium isotope composition in the marine environment: a preliminary report. Geochim. Cosmochim. Acta 52, 1711–1717.

Chang, V.-T.-C., Williams, R.J.P., Makishima, A., Belshawl, N.S., O'Nions, R.K., 2004. Mg and Ca isotope fractionation during $CaCO_3$ biomineralisation. Biochem. Biophys. Res. Commun. 323, 79–85.

Charrieau, L.M., Rollion-Bard, C., Terbrueggen, A., Wilson, D.J., Pogge von Strandmann, P.A.E., Misra, S., Bijma, J., 2023. Controls on lithium incorporation and isotopic fractionation in large benthic foraminifera. Minerals 13, 127.

Chave, K.E., 1962. Factors influencing the mineralogy of carbonate sediments. Limnol. Oceanogr. 7, 218–223.

Chen, D., Thibon, F., Felbacq, A., Weppe, L., Metian, M., Vigier, N., 2023. Coupled survey of lithium isotopes and Li/Ca in biogenic and inorganic carbonates. Earth Sci. Rev. 244, 104500.

Chen, S., Littley, E.F.M., Rae, J.W.B., Charles, C.D., Guan, Y., Adkins, J.F., 2023. Coherent tracer correlations in deep-sea corals and implications for biomineralization mechanisms underlying vital effects. Geochim. Cosmochim. Acta 343, 304–322.

Cohen, A.L., Gaetani, G.A., Lundälv, T., Corliss, B.H., George, R.Y., 2006. Compositional variability in a cold-water scleractinian, Lophelia pertusa: new insights into "vital effects". Geochem. Geophys. Geosyst. 7.

Cohen, A.L., McConnaughey, T.A., 2003. Geochemical perspectives on coral mineralization. Rev. Mineral. Geochem. 54, 151–187.

Craig, H., 1961. Standard for reporting concentrations of deuterium and oxygen-18 in natural waters. Science 133, 1833–1834.

Craig, H., 1953. The geochemistry of the stable carbon isotopes. Geochim. Cosmochim. Acta 3, 53–92.

Cuny-Guirriec, K., Douville, E., Reynaud, S., Allemand, D., Bordier, L., Canesi, M., Mazzoli, C., Taviani, M., Canese, S., McCulloch, M., Trotter, J., Rico-Esenaro, S.D., Sanchez-Cabeza, J.-A., Ruiz-Fernández, A.C., Carricart-Ganivet, J.P., Scott, P.M., Sadekov, A., Montagna, P., 2019. Coral Li/Mg thermometry: caveats and constraints. Chem. Geol. 523, 162–178.

Davis, K.J., Dove, P.M., De Yoreo, J.J., 2000. The role of Mg^{2+} as an impurity in calcite growth. Science 290, 1134–1137.

Day, C.C., Pogge von Strandmann, P.A.E., Mason, A.J., 2021. Lithium isotopes and partition coefficients in inorganic carbonates: proxy calibration for weathering reconstruction. Geochim. Cosmochim. Acta 305, 243–262.

Delaney, M.L., Popp, B.N., Lepzelter, C.G., Anderson, T.F., 1989. Lithium-to-calcium ratios in Modern, Cenozoic, and Paleozoic articulate brachiopod shells. Paleoceanography 4, 681–691.

Dellinger, M., Gaillardet, J., Bouchez, J., Calmels, D., Louvat, P., Dosseto, A., Gorge, C., Alanoca, L., Maurice, L., 2015. Riverine Li isotope fractionation in the Amazon River basin controlled by the weathering regimes. Geochim. Cosmochim. Acta 164, 71–93.

Dellinger, M., Hardisty, D.S., Planavsky, N.J., Gill, B.C., Kalderon-Asael, B., Asael, D., Croissant, T., Swart, P.K., West, A.J., 2020. The effects of diagenesis on lithium isotope ratios of shallow marine carbonates. Am. J. Sci. 320.

Dellinger, M., West, A.J., Paris, G., Adkins, J.F., Pogge von Strandmann, P.A.E., Ullmann, C.V., Eagle, R.A., Freitas, P., Bagard, M.-L., Ries, J.B., Corsetti, F.A., Perez-Huerta, A., Kampf, A.R., 2018. The Li isotope composition of marine biogenic carbonates: patterns and mechanisms. Geochim. Cosmochim. Acta 236, 315–335.

Dissard, D., Nehrke, G., Reichart, G.J., Bijma, J., 2010. Impact of seawater pCO_2 on calcification and Mg/Ca and Sr/Ca ratios in benthic foraminifera calcite: results from culturing experiments with *Ammonia tepida*. Biogeosciences 7, 81–93.

Dunn, R.P., Eggleston, D.B., Lindquist, N., 2014. Effects of substrate type on demographic rates of Eastern Oyster (*Crassostrea virginica*). J. Shellfish. Res. 33, 177–185.

Dwyer, G.S., Cronin, T.M., Baker, P.A., 2002. Trace elements in Marine Ostracodes. In: The Ostracoda: Applications in Quaternary. Research American Geophysical Union (AGU), pp. 205–225.
Eble A.F., Scro R., 1996. General anatomy. In The Eastern Oyster *Crassostrea virginica*. pp. 19–73.
Epstein, S., Buchsbaum, R., Lowenstam, H., Urey, H.C., 1951. Carbonate-water isotopic temperature scale. GSA Bull. Georg. Acad. Sci. 62, 417–426.
Erez, J., 2003. The source of ions for biomineralization in foraminifera and their implications for paleoceanographic proxies. Rev. Mineral. Geochem. 54, 115–149.
Fantle, M.S., Barnes, B.D., Lau, K.V., 2020. The role of diagenesis in shaping the geochemistry of the marine carbonate record. Annu. Rev. Earth Planet. Sci. 48, 549–583.
Farkaš, J., Böhm, F., Wallmann, K., Blenkinsop, J., Eisenhauer, A., van Geldern, R., Munnecke, A., Voigt;, S., Veizer, J., 2007. Calcium isotope record of Phanerozoic oceans: Implications for chemical evolution of seawater and its causative mechanisms. Geochim. Cosmochim. Acta 71, 5117–5134.
Fowell, S.E., Sandford, K., Stewart, J.A., Castillo, K.D., Ries, J.B., Foster, G.L., 2016. Intrareef variations in Li/Mg and Sr/Ca sea surface temperature proxies in the Caribbean reef-building coral *Siderastrea siderea*. Paleoceanography 31, 1315–1329.
Freitas, P.S., Clarke, L.J., Kennedy, H., Richardson, C.A., Abrantes, F., 2006. Environmental and biological controls on elemental (Mg/Ca, Sr/Ca and Mn/Ca) ratios in shells of the king scallop *Pecten maximus*. Geochim. Cosmochim. Acta 70, 5119–5133.
Füger, A., Konrad, F., Leis, A., Dietzel, M., Mavromatis, V., 2019. Effect of growth rate and pH on lithium incorporation in calcite. Geochim. Cosmochim. Acta 248, 14–24.
Füger, A., Kuessner, M., Rollion-Bard, C., Leis, A., Magna, T., Dietzel, M., Mavromatis, V., 2022. Effect of growth rate and pH on Li isotope fractionation during its incorporation in calcite. Geochim. Cosmochim. Acta 323, 276–290.
Gabitov, R.I., Schmitt, A.K., Rosner, M., McKeegan, K.D., Gaetani, G.A., Cohen, A.L., Watson, E.B., Harrison, T.M., 2011. In situ δ7Li, Li/Ca, and Mg/Ca analyses of synthetic aragonites. Geochem. Geophys. Geosyst. 12.
Gabitov, R.I., Watson, E.B., 2006. Partitioning of strontium between calcite and fluid. Geochem. Geophys. Geosyst. 7.
Gaetani, G.A., Cohen, A.L., 2006. Element partitioning during precipitation of aragonite from seawater: a framework for understanding paleoproxies. Geochim. Cosmochim. Acta 70, 4617–4634.
Gagan, M.K., Ayliffe, L.K., Hopley, D., Cali, J.A., Mortimer, G.E., Chappell, J., McCulloch, M.T., Head, M.J., 1998. Temperature and surface-ocean water balance of the mid-holocene tropical Western Pacific. Science 279, 1014–1018.
Gillikin, D.P., Lorrain, A., Navez, J., Taylor, J.W., André, L., Keppens, E., Baeyens, W., Dehairs, F., 2005. Strong biological controls on Sr/Ca ratios in aragonitic marine bivalve shells. Geochem. Geophys Geosyst. 6.
Griffith, E.M., Paytan, A., Kozdon, R., Eisenhauer, A., Ravelo, A.C., 2008. Influences on the fractionation of calcium isotopes in planktonic foraminifera. Earth Planet. Sci. Lett. 268, 124–136.
Gussone, N., Böhm, F., Eisenhauer, A., Dietzel, M., Heuser, A., Teichert, B.M.A., Reitner, J., Wörheide, G., Dullo, W.-C., 2005. Calcium isotope fractionation in calcite and aragonite. Geochim. Cosmochim. Acta 69, 4485–4494.
Gussone, N., Eisenhauer, A., Heuser, A., Dietzel, M., Bock, B., Böhm, F., Spero, H.J., Lea, D.W., Bijma, J., Nägler, T.F., 2003. Model for kinetic effects on calcium isotope fractionation (δ^{44}Ca) in inorganic aragonite and cultured planktonic foraminifera. Geochim. Cosmochim. Acta 67, 1375–1382.
Gussone, N., Filipsson, H.L., Kuhnert, H., 2016. Mg/Ca, Sr/Ca and Ca isotope ratios in benthonic foraminifers related to test structure, mineralogy and environmental controls. Geochim. Cosmochim. Acta 173, 142–159.
Gussone, N., Langer, G., Thoms, S., Nehrke, G., Eisenhauer, A., Riebesell, U., Wefer, G., 2006. Cellular calcium pathways and isotope fractionation in *Emiliania huxleyi*. Geology 34, 625.
Haase-Schramm, A., Böhm, F., Eisenhauer, A., Dullo, W.-C., Joachimski, M.M., Hansen, B., Reitner, J., 2003. Sr/Ca ratios and oxygen isotopes from sclerosponges: temperature history of the Caribbean mixed layer and thermocline during the little ice age. Paleoceanography 18.
Hall, J.M., Chan, L.-H., McDonough, W.F., Turekian, K.K., 2005. Determination of the lithium isotopic composition of planktic foraminifera and its application as a paleo-seawater proxy. Mar. Geol. 217, 255–265.
Hartley, G., Mucci, A., 1996. The influence of pCO_2 on the partitioning of magnesium in calcite overgrowths precipitated from artificial seawater at 25° and 1 atm total pressure. Geochim. Cosmochim. Acta 60, 315–324.
Hathorne, E.C., Felis, T., Suzuki, A., Kawahata, H., Cabioch, G., 2013. Lithium in the aragonite skeletons of massive *Porites* corals: a new tool to reconstruct tropical sea surface temperatures. Paleoceanography 28, 143–152.
Hathorne, E.C., James, R.H., 2006. Temporal record of lithium in seawater: a tracer for silicate weathering? Earth Planet Sci. Lett. 246, 393–406.
Heinemann, A., Fietzke, J., Eisenhauer, A., Zumholz, K., 2008. Modification of Ca isotope and trace metal composition of the major matrices involved in shell formation of *Mytilus edulis*. Geochem. Geophys Geosyst. 9.
Heuser, A., Eisenhauer, A., Böhm, F., Wallmann, K., Gussone, N., Pearson, P., Nägler, T., Dullo, W.-C., 2005. Calcium isotope ($\delta^{44/40}$Ca) variations of Neogene planktonic foraminifera: paleoceanography. Paleoceanography 20.
Hippler, D., Buhl, D., Witbaard, R., Richter, D.K., Immenhauser, A., 2009. Towards a better understanding of magnesium-isotope ratios from marine skeletal carbonates. Geochim. Cosmochim. Acta 73, 6134–6146.
Hippler, D., Witbaard, R., van Aken, H.M., Buhl, D., Immenhauser, A., 2013. Exploring the calcium isotope signature of *Arctica islandica* as an environmental proxy using laboratory- and field-cultured specimens. Palaeogeogr. Palaeoclimatol. Palaeoecol. 373, 75–87.
Hite, C., Uchikawa, J., Misra, S., Satya, C.I.V., Chanda, P., Zeebe, R.E., 2025. Strong and persistent mineral-specific lithium isotope fractionation: no discernable kinetic isotope effects during inorganic calcite and aragonite precipitation. Geochim. Cosmochim. Acta 397, 37–52.
Hofmann, A.E., Bourg, I.C., DePaolo, D.J., 2012. Ion desolvation as a mechanism for kinetic isotope fractionation in aqueous systems. Proc. Natl. Acad. Sci. 109, 18689–18694.
Holmden, C., Papanastassiou, D.A., Blanchon, P., Evans, S., 2012. $\delta^{44/40}$Ca variability in shallow water carbonates and the impact of submarine groundwater discharge on Ca-cycling in marine environments. Geochim. Cosmochim. Acta 83, 179–194.
Howson, M.R., Pethybridge, A.D., House, W.A., 1987. Synthesis and distribution coefficient of low-magnesium calcites. Chem. Geol. 64, 79–87.
Hu, X., Yao, H., McCutcheon, M.R., Dias, L., Staryk, C.J., Wetz, M.S., Montagna, P.A., 2022. Aragonite saturation states in estuaries along a climate gradient in the northwestern Gulf of Mexico. Front. Environ Sci 10.
Huang, Y., Fairchild, I.J., 2001. Partitioning of Sr^{2+} and Mg^{2+} into calcite under karst-analogue experimental conditions. Geochim. Cosmochim. Acta 65, 47–62.
Huh, Y., Chan, L.-H., Zhang, L., Edmond, J.M., 1998. Lithium and its isotopes in major world rivers: implications for weathering and the oceanic budget. Geochim. Cosmochim. Acta 62, 2039–2051.
Immenhauser, A., Schöne, B.R., Hoffmann, R., Niedermayr, A., 2016. Mollusc and brachiopod skeletal hard parts: Intricate archives of their marine environment. Sedimentology 63, 1–59.
James, R.H., Palmer, M.R., 2000. The lithium isotope composition of international rock standards. Chem. Geol. 166, 319–326.
Jochum, K.P., Nohl, U., Herwig, K., Lammel, E., Stoll, B., Hofmann, A.W., 2005. GeoReM: a new geochemical database for reference materials and isotopic standards. Geostand. Geoanalytical Res. 29, 333–338.
John, C.M., Bowen, D., 2016. Community software for challenging isotope analysis: first applications of "Easotope" to clumped isotopes. Rapid Commun. Mass Spectrom. RCM 30, 2285–2300.
John, S.G., Adkins, J.F., 2010. Analysis of dissolved iron isotopes in seawater. Mar. Chem. 119, 65–76.
Jones, C.E., Jenkyns, H.C., Hesselbo, S.P., 1994. Strontium isotopes in Early Jurassic seawater. Geochim. Cosmochim. Acta 58, 1285–1301.
Kasemann, S.A., Schmidt, D.N., Pearson, P.N., Hawkesworth, C.J., 2008. Biological and ecological insights into Ca isotopes in planktic foraminifers as a palaeotemperature proxy. Earth Planet. Sci. Lett. 271, 292–302.
Kendall, C., Coplen, T.B., 2001. Distribution of oxygen-18 and deuterium in river waters across the United States. Hydrol. Process. 15, 1363–1393.
Killingley, J.S., Berger, W.H., 1979. Stable isotopes in a Mollusk shell: detection of upwelling events. Science.
Kipp, M.A., Gao, A., Tissot, F.L.H., Adkins, J.F., 2024. $^{238}U/^{235}U$ in deep-sea corals reflects limited expansion of seafloor anoxia in last ice age. Geochem. Perspect. Lett. 33, 32–37.
Kipp, M.A., Piccirillo, L.F., Peters, D., 2025. High precision selenium isotope analysis using a Nu Sapphire collision–reaction cell MC-ICP-MS. J. Anal. At. Spectrom 40, 2792–2802.
Klein, R.T., Lohmann, K.C., Thayer, C.W., 1996. Sr/Ca and $^{13}C/^{12}C$ ratios in skeletal calcite of *Mytilus trossulus*: covariation with metabolic rate, salinity, and carbon isotopic composition of seawater. Geochim. Cosmochim. Acta 60, 4207–4221.
Knight, A.W., Harvey, J.A., Shohel, M., Lu, P., Cummings, D., Ilgen, A.G., 2023. The combined effects of Mg^{2+} and Sr^{2+} incorporation during $CaCO_3$ precipitation and crystal growth. Geochim. Cosmochim. Acta 345, 16–33.
Korte, C., Hesselbo, S.P., 2011. Shallow marine carbon and oxygen isotope and elemental records indicate icehouse-greenhouse cycles during the Early Jurassic. Paleoceanography 26.
Korte, C., Hesselbo, S.P., Jenkyns, H.C., Rickaby, R.E.M., Spötl, C., 2009. Palaeoenvironmental significance of carbon- and oxygen-isotope stratigraphy of marine Triassic–Jurassic boundary sections in SW Britain. J. Geol. Soc. 166, 431–445.
Lahann, R.W., 1978. A chemical model for calcite crystal growth and morphology control. J. Sediment. Res. 48, 337–347.
Li, W., Chakraborty, S., Beard, B.L., Romanek, C.S., Johnson, C.M., 2012. Magnesium isotope fractionation during precipitation of inorganic calcite under laboratory conditions. Earth Planet. Sci. Lett. 333–334, 304–316.
Liu, S., Li, W., Su, B., Gao, B., Wang, J., Wang, C., Luo, Y., Yan, L., Zhao, Y., 2023. High-precision lithium isotopic analysis using the Nu Sapphire MC-ICP-MS. J. Anal. At. Spectrom 38, 656–666.
Mackenzie, C.L., 2007. Causes underlying the historical decline in Eastern Oyster (*Crassostrea virginica* Gmelin, 1791) landings. J. Shellfish. Res. 26, 927–938.
Marchitto, T.M., Bryan, S.P., Doss, W., McCulloch, M.T., Montagna, P., 2018. A simple biomineralization model to explain Li, Mg, and Sr incorporation into aragonitic foraminifera and corals. Earth Planet. Sci. Lett. 481, 20–29.
Marriott, C.S., Henderson, G.M., Belshaw, N.S., Tudhope, A.W., 2004a. Temperature dependence of δ^7Li, δ^{44}Ca and Li/Ca during growth of calcium carbonate. Earth Planet. Sci. Lett. 222, 615–624.
Marriott, C.S., Henderson, G.M., Crompton, R., Staubwasser, M., Shaw, S., 2004b. Effect of mineralogy, salinity, and temperature on Li/Ca and Li isotope composition of calcium carbonate. Chem. Geol. 212, 5–15.
Marshall, J.D., 1992. Climatic and oceanographic isotopic signals from the carbonate rock record and their preservation. Geol. Mag. 129, 143–160.
Mavromatis, V., Gautier, Q., Bosc, O., Schott, J., 2013. Kinetics of Mg partition and Mg stable isotope fractionation during its incorporation in calcite. Geochim. Cosmochim. Acta 114, 188–203.

McCrea, J.M., 1950. On the isotopic chemistry of carbonates and a paleotemperature scale. J. Chem. Phys. 18, 849–857.
Millero, F.J., 2016. Chemical Oceanography, 4th ed. CRC Press, Boca Raton.
Millot, R., Guerrot, C., Vigier, N., 2004. Accurate and high-precision measurement of lithium isotopes in two reference materials by MC-ICP-MS. Geostand. Geoanal. Res. 28, 153–159.
Millot, R., Vigier, N., Gaillardet, J., 2010. Behaviour of lithium and its isotopes during weathering in the Mackenzie Basin, Canada. Geochim. Cosmochim. Acta 74, 3897–3912.
Misra, S., Froelich, P.N., 2012. Lithium isotope history of cenozoic seawater: changes in silicate weathering and reverse weathering. Science 335, 818–823.
Misra, S., Froelich, P.N., 2009. Measurement of lithium isotope ratios by quadrupole-ICP-MS: application to seawater and natural carbonates. J. Anal. At. Spectrom 24, 1524–1533.
Montagna, P., McCulloch, M., Douville, E., López, C.M., Trotter, J., Rodolfo-Metalpa, R., Dissard, D., Ferrier-Pagès, C., Frank, N., Freiwald, A., Goldstein, S., Mazzoli, C., Reynaud, S., Rüggeberg, A., Russo, S., Taviani, M., 2014. Li/Mg systematics in scleractinian corals: calibration of the thermometer. Geochim. Cosmochim. Acta 132, 288–310.
Mook, W.G., Koene, B.K.S., 1975. Chemistry of dissolved inorganic carbon in estuarine and coastal brackish waters. Estuar. Coast. Mar. Sci. 3, 325–336.
Morse, J.W., Arvidson, R.S., Lüttge, A., 2007. Calcium carbonate formation and dissolution. Chem. Rev. 107, 342–381.
Mortyn, P.G., Elderfield, H., Anand, P., Greaves, M., 2005. An evaluation of controls on planktonic foraminiferal Sr/Ca: comparison of water column and core-top data from a North Atlantic transect. Geochem. Geophys Geosyst. 6.
Mosley, L.M., Peake, B.M., Hunter, K.A., 2010. Modelling of pH and inorganic carbon speciation in estuaries using the composition of the river and seawater end members. Environ Model Softw. 25, 1658–1663.
Mucci, A., 1987. Influence of temperature on the composition of magnesian calcite overgrowths precipitated from seawater. Geochim. Cosmochim. Acta 51, 1977–1984.
Mucci, A., Morse, J.W., 1983. The incorporation of Mg^{2+} and Sr^{2+} into calcite overgrowths: influences of growth rate and solution composition. Geochim. Cosmochim. Acta 47, 217–233.
Murphy, J.G., Ahm, A.-S.-C., Swart, P.K., Higgins, J.A., 2022. Reconstructing the lithium isotopic composition (δ^7Li) of seawater from shallow marine carbonate sediments. Geochim. Cosmochim. Acta 337, 140–154.
Murphy, M.J., Porcelli, D., Pogge von Strandmann, P.A.E., Hirst, C.A., Kutscher, L., Katchinoff, J.A., Mörth, C.-M., Maximov, T., Andersson, P.S., 2019. Tracing silicate weathering processes in the permafrost-dominated Lena River watershed using lithium isotopes. Geochim. Cosmochim. Acta 245, 154–171.
Okumura, M., Kitano, Y., 1986. Coprecipitation of alkali metal ions with calcium carbonate. Geochim. Cosmochim. Acta 50, 49–58.
O'Leary, M.H., 1988. Carbon isotopes in photosynthesis. Bioscience 38, 328–336.
Oliveira, A.P., Cabeçadas, G., Mateus, M.D., 2017. Inorganic carbon distribution and CO_2 fluxes in a large European estuary (Tagus, Portugal). Sci. Rep. 7, 7376.
Omarjee, A., Taljaard, S., Ramjukadh, C.-L., van Niekerk, L., 2021. pH variability in catchment flows to estuaries – a South African perspective. Estuar. Coast. Shelf Sci. 262, 107605.
Oomori, T., Kaneshima, H., Maezato, Y., Kitano, Y., 1987. Distribution coefficient of Mg^{2+} ions between calcite and solution at 10-50°C. Mar. Chem. 20, 327–336.
Ortega, S., 1981. Environmental stress, competition and dominance of *Crassostrea virginica* near Beaufort, North Carolina, USA. Mar. Biol. 62, 47–56.
Ortega, S., Sutherland, J.P., 1992. Recruitment and growth of the Eastern oyster, *Crassostrea virginica*, in North Carolina. Estuaries 15, 158–170.
Patterson, W.P., Walter, L.M., 1994. Syndepositional diagenesis of modern platform carbonates: evidence from isotopic and minor element data. Geology 22, 127–130.
Planchon, F., Poulain, C., Langlet, D., Paulet, Y.-M., André, L., 2013. Mg-isotopic fractionation in the manila clam (*Ruditapes philippinarum*): New insights into Mg incorporation pathway and calcification process of bivalves. Geochim. Cosmochim. Acta 121, 374–397.
Pogge von Strandmann, P.A.E., 2008. Precise magnesium isotope measurements in core top planktic and benthic foraminifera. Geochem. Geophys Geosyst. 9.
Pogge von Strandmann, P.A.E., Burton, K.W., James, R.H., van Calsteren, P., Gíslason, S. R., Mokadem, F., 2006. Riverine behaviour of uranium and lithium isotopes in an actively glaciated basaltic terrain. Earth Planet. Sci. Lett. 251, 134–147.
Pogge von Strandmann, P.A.E., Frings, P.J., Murphy, M.J., 2017. Lithium isotope behaviour during weathering in the Ganges Alluvial Plain. Geochim. Cosmochim. Acta 198, 17–31.
Pogge von Strandmann, P.A.E., Jenkyns, H.C., Woodfine, R.G., 2013. Lithium isotope evidence for enhanced weathering during Oceanic Anoxic Event 2. Nat. Geosci. 6, 668–672.
Pogge von Strandmann, P.A.E., Kasemann, S.A., Wimpenny, J.B., 2020. Lithium and lithium isotopes in earth's surface cycles. Elements 16, 253–258.
Pretet, C., Samankassou, E., Felis, T., Reynaud, S., Böhm, F., Eisenhauer, A., Ferrier-Pagès, C., Gattuso, J.-P., Camoin, G., 2013. Constraining calcium isotope fractionation ($\delta^{44/40}$Ca) in modern and fossil scleractinian coral skeleton. Chem. Geol. 340, 49–58.
Purton, L.M.A., Shields, G.A., Brasier, M.D., Grime, G.W., 1999. Metabolism controls Sr/Ca ratios in fossil aragonitic mollusks. Geology 27, 1083–1086.
Raddatz, J., Liebetrau, V., Rüggeberg, A., Hathorne, E., Krabbenhöft, A., Eisenhauer, A., Böhm, F., Vollstaedt, H., Fietzke, J., López, C.M., Freiwald, A., Dullo, W.-Chr., 2013. Stable Sr-isotope, Sr/Ca, Mg/Ca, Li/Ca and Mg/Li ratios in the scleractinian cold-water coral *Lophelia pertusa*. Chem. Geol. 352, 143–152.
Rathburn, A.E., De Deckker, P., 1997. Magnesium and strontium compositions of recent benthic foraminifera from the Coral Sea, Australia and Prydz Bay. Antarctica. Mar. Micropaleontol. 32, 231–248.
Reisdorph, S.C., Mathis, J.T., 2014. The dynamic controls on carbonate mineral saturation states and ocean acidification in a glacially dominated estuary. Estuar. Coast. Shelf Sci. 144, 8–18.
Ries, J.B., 2010. Review: geological and experimental evidence for secular variation in seawater Mg/Ca (calcite-aragonite seas) and its effects on marine biological calcification. Biogeosciences 7, 2795–2849.
Rollion-Bard, C., Blamart, D., 2015. Possible controls on Li, Na, and Mg incorporation into aragonite coral skeletons. Chem. Geol. 396, 98–111.
Rollion-Bard, C., Vigier, N., Meibom, A., Blamart, D., Reynaud, S., Rodolfo-Metalpa, R., Martin, S., Gattuso, J.-P., 2009. Effect of environmental conditions and skeletal ultrastructure on the Li isotopic composition of scleractinian corals. Earth Planet. Sci. Lett. 286, 63–70.
Ross, C.L., DeCarlo, T.M., McCulloch, M.T., 2019. Calibration of Sr/Ca, Li/Mg and Sr-U paleothermometry in branching and foliose corals. Paleoceanogr. Paleoclimatology 34, 1271–1291.
Russell, A.D., Hönisch, B., Spero, H.J., Lea, D.W., 2004. Effects of seawater carbonate ion concentration and temperature on shell U, Mg, and Sr in cultured planktonic foraminifera. Geochim. Cosmochim. Acta 68, 4347–4361.
Saenger, C., Wang, Z., 2014. Magnesium isotope fractionation in biogenic and abiogenic carbonates: implications for paleoenvironmental proxies. Quat. Sci. Rev. 90, 1–21.
Saenger, C., Wang, Z., Gaetani, G., Cohen, A., Lough, J.M., 2013. The influence of temperature and vital effects on magnesium isotope variability in *Porites* and *Astrangia* corals. Chem. Geol. 360–361, 105–117.
Seyedali, M., Coogan, L.A., Gillis, K.M., 2021. The effect of solution chemistry on elemental and isotopic fractionation of lithium during inorganic precipitation of calcite. Geochim. Cosmochim. Acta 311, 102–118.
Shi, W., Zhai, W., 2025. Combining summertime freshwater inputs and oxygen consumption impacts on coastal low aragonite saturation state: Case of the Pearl River Estuary, South China. Mar. Pollut. Bull. 219, 118293.
Sime, N.G., De La Rocha, C.L., Galy, A., 2005. Negligible temperature dependence of calcium isotope fractionation in 12 species of planktonic foraminifera. Earth Planet. Sci. Lett. 232, 51–66.
Skulan, J., DePaolo, D.J., Owens, T.L., 1997. Biological control of calcium isotopic abundances in the global calcium cycle. Geochim. Cosmochim. Acta 61, 2505–2510.
Steuber, T., Buhl, D., 2006. Calcium-isotope fractionation in selected modern and ancient marine carbonates. Geochim. Cosmochim. Acta 70, 5507–5521.
Stewart, J.A., Robinson, L.F., Day, R.D., Strawson, I., Burke, A., Rae, J.W.B., Spooner, P. T., Samperiz, A., Etnoyer, P.J., Williams, B., Paytan, A., Leng, M.J., Häussermann, V., Wickes, L.N., Bratt, R., Pryer, H., 2020. Refining trace metal temperature proxies in cold-water scleractinian and stylasterid corals. Earth Planet. Sci. Lett. 545, 116412.
Surge, D., Lohmann, K.C., Dettman, D.L., 2001. Controls on isotopic chemistry of the American oyster, *Crassostrea virginica*: implications for growth patterns. Palaeogeogr. Palaeoclimatol. Palaeoecol. 172, 283–296.
Tang, J., Köhler, S.J., Dietzel, M., 2008. Sr^{2+}/Ca^{2+} and $^{44}Ca/^{40}Ca$ fractionation during inorganic calcite formation: I. Sr Incorporation. Geochim. Cosmochim. Acta 72, 3718–3732.
Teng, F.-Z., McDonough, W.F., Rudnick, R.L., Dalpé, C., Tomascak, P.B., Chappell, B.W., Gao, S., 2004. Lithium isotopic composition and concentration of the upper continental crust. Geochim. Cosmochim. Acta 68, 4167–4178.
Thébault, J., Chauvaud, L., 2013. Li/Ca enrichments in great scallop shells (*Pecten maximus*) and their relationship with phytoplankton blooms. Palaeogeogr. Palaeoclimatol. Palaeoecol. 373, 108–122.
Tomascak, P.B., Magna, T., Dohmen, R., 2016. Advances in Lithium Isotope Geochemistry. Springer International Publishing, Cham.
Ullmann, C.V., Böhm, F., Rickaby, R.E.M., Wiechert, U., Korte, C., 2013. The Giant Pacific Oyster (*Crassostrea gigas*) as a modern analog for fossil ostreoids: isotopic (Ca, O, C) and elemental (Mg/Ca, Sr/Ca, Mn/Ca) proxies. Geochem. Geophys. Geosyst. 14, 4109–4120.
Ullmann, C.V., Frei, R., Korte, C., Lüter, C., 2017. Element/Ca, C and O isotope ratios in modern brachiopods: species-specific signals of biomineralization. Chem. Geol. 460, 15–24.
Ullmann, C.V., Korte, C., 2015. Diagenetic alteration in low-Mg calcite from macrofossils: a review. Geol. Q. 59, 10.7306/gq.1217.
Ullmann, C.V., Wiechert, U., Korte, C., 2010. Oxygen isotope fluctuations in a modern North Sea oyster (*Crassostrea gigas*) compared with annual variations in seawater temperature: implications for palaeoclimate studies. Chem. Geol. 277, 160–166.
Ulrich, R.N., Guillermic, M., Campbell, J., Hakim, A., Han, R., Singh, S., Stewart, J.D., Román-Palacios, C., Carroll, H.M., De Corte, I., Gilmore, R.E., Doss, W., Tripati, A., Ries, J.B., Eagle, R.A., 2021. Patterns of element incorporation in calcium carbonate biominerals recapitulate phylogeny for a diverse range of marine calcifiers. Front. Earth Sci. 9.
Veizer, J., 1983. Chemical diagenesis of carbonates: theory and application of trace element technique. In Stable Isotopes in Sedimentary Geology (eds. M. A. Arthur, T. F. Anderson, I. R. Kaplan, Jan Veizer, and L. S. Land). SEPM Society for Sedimentary Geology. p. 0.
Vigier, N., Rollion-Bard, C., Levenson, Y., Erez, J., 2015. Lithium isotopes in foraminifera shells as a novel proxy for the ocean dissolved inorganic carbon (DIC). Comptes Rendus Geosci. 347, 43–51.
de Villiers, S., Nelson, B.K., Chivas, A.R., 1995. Biological controls on coral Sr/Ca and δ^{18}O reconstructions of sea surface temperatures. Science 269, 1247–1249.
Volkov, A.G., Paula, S., Deamer, D.W., 1997. Two mechanisms of permeation of small neutral molecules and hydrated ions across phospholipid bilayers. Bioelectrochem. Bioenerg. 42, 153–160.

Wang, Z., Hu, P., Gaetani, G., Liu, C., Saenger, C., Cohen, A., Hart, S., 2013. Experimental calibration of Mg isotope fractionation between aragonite and seawater. Geochim. Cosmochim. Acta 102, 113–123.
Watabe, N., Wilbur, K.M., 1960. Influence of the organic matrix on crystal type in molluscs. Nature 188, 334.
Wefer, G., Berger, W.H., 1991. Isotope paleontology: growth and composition of extant calcareous species. Mar. Geol. 100, 207–248.
Wierzbowski, H., Joachimski, M., 2007. Reconstruction of late Bajocian–Bathonian marine palaeoenvironments using carbon and oxygen isotope ratios of calcareous fossils from the Polish Jura Chain (central Poland). Palaeogeogr. Palaeoclimatol. Palaeoecol. 254, 523–540.
Wombacher, F., Eisenhauer, A., Böhm, F., Gussone, N., Regenberg, M., Dullo, W.-Chr., Rüggeberg, A., 2011. Magnesium stable isotope fractionation in marine biogenic calcite and aragonite. Geochim. Cosmochim. Acta 75, 5797–5818.
Yan, J., Lin, Q., Poh, S.C., Li, Y., Zhan, L., 2020. Underway measurement of dissolved inorganic carbon (DIC) in Estuarine Waters. J. Mar. Sci. Eng. 8, 765.
Yoshimura, T., Tanimizu, M., Inoue, M., Suzuki, A., Iwasaki, N., Kawahata, H., 2011. Mg isotope fractionation in biogenic carbonates of deep-sea coral, benthic foraminifera, and hermatypic coral. Anal. Bioanal. Chem. 401, 2755–2769.
Zeebe, R.E., Sanyal, A., 2002. Comparison of two potential strategies of planktonic foraminifera for house building: Mg^{2+} or H^{+} removal? Geochim. Cosmochim. Acta 66, 1159–1169.
Zhu, P., Macdougall, J.D., 1998. Calcium isotopes in the marine environment and the oceanic calcium cycle. Geochim. Cosmochim. Acta 62, 1691–1698.